Chemistry in the GG Tau A Disk: Constraints from H 2 D + , N 2 H + , and DCO + High Angular Resolution ALMA Observations

Parashmoni Kashyap, Liton Majumdar, Anne Dutrey, Stéphane Guilloteau, Karen Willacy, Edwige Chapillon, Richard Teague, Dmitry Semenov, Thomas Henning, Neal Turner, et al.

The Astrophysical Journal, 976:258 (22pp), 2024 December 1 https://doi.org/10.3847/1538-4357/ad815c

Chemistry in the GG Tau A Disk: Constraints from H_2D^+, N_2H^+, and DCO^+ High Angular Resolution ALMA Observations

Parashmoni Kashyap[1,2], Liton Majumdar[1,2], Anne Dutrey[3], Stéphane Guilloteau[3], Karen Willacy[4], Edwige Chapillon[3,5], Richard Teague[6], Dmitry Semenov[7,8], Thomas Henning[7], Neal Turner[4], Raghvendra Sahai[4], Ágnes Kóspál[7,9,10], Audrey Coutens[11], V. Piétu[5], Pierre Gratier[3], Maxime Ruaud[12,13], N. T. Phuong[14], E. Di Folco[3], Chin-Fei Lee[15], and Y.-W. Tang[15]

[1] Exoplanets and Planetary Formation Group, School of Earth and Planetary Sciences, National Institute of Science Education and Research, Jatni 752050, Odisha, India; liton@niser.ac.in, dr.liton.majumdar@gmail.com
[2] Homi Bhabha National Institute, Training School Complex, Anushaktinagar, Mumbai 400094, India
[3] Laboratoire d'Astrophysique de Bordeaux, Université de Bordeaux, CNRS, B18N, Allée Geoffroy Saint-Hilaire, F-33615 Pessac, France
[4] Jet Propulsion Laboratory, California Institute of Technology, 4800 Oak Grove Dr., Pasadena, CA 91109, USA
[5] Institut de Radioastronomie Millimétrique (IRAM), 300 rue de la Piscine, F-38406 Saint-Martin d'Héres, France
[6] Department of Earth, Atmospheric, and Planetary Sciences, Massachusetts Institute of Technology, Cambridge, MA 02139, USA
[7] Max Planck Institute for Astronomy, Königstuhl 17, D-69117 Heidelberg, Germany
[8] Department of Chemistry, Ludwig Maximilian University, Butenandtstr. 5-13, D-81377 Munich, Germany
[9] Konkoly Observatory, HUN-REN Research Centre for Astronomy and Earth Sciences, CSFK, MTA Centre of Excellence, Konkoly-Thege Miklós út 15-17, 1121 Budapest, Hungary
[10] Institute of Physics and Astronomy, ELTE Eötvös Loránd University, Pázmány Péter sétány 1/A, 1117 Budapest, Hungary
[11] Institut de Recherche en Astrophysique et Planétologie (IRAP), Université de Toulouse, UT3-PS, CNRS, CNES, 9 av. du Colonel Roche, 31028 Toulouse Cedex 4, France
[12] NASA Ames Research Center, Moffett Field, CA 94035, USA
[13] Carl Sagan Center, SETI Institute, Mountain View, CA 94035, USA
[14] Department of Astrophysics, Vietnam National Space Center, Vietnam Academy of Science and Techonology, 18 Hoang Quoc Viet, Cau Giay, Hanoi, Vietnam
[15] Academia Sinica Institute of Astronomy and Astrophysics, PO Box 23-141, Taipei 106, Taiwan
Received 2024 February 17; revised 2024 September 23; accepted 2024 September 26; published 2024 November 27

Abstract

Resolved molecular line observations are essential for gaining insight into the physical and chemical structure of protoplanetary disks, particularly in cold, dense regions where planets form and acquire their chemical compositions. However, tracing these regions is challenging because most molecules freeze onto grain surfaces and are not observable in the gas phase. We investigated cold molecular chemistry in the triple stellar T Tauri disk GG Tau A, which harbours a massive gas and dust ring and an outer disk, using Atacama Large Millimeter/submillimeter Array (ALMA) Band 7 observations. We present high angular resolution maps of N_2H^+ and DCO^+ emission, with upper limits reported for H_2D^+, ^{13}CS, and SO_2. The radial intensity profile of N_2H^+ shows most emission near the ring's outer edge, while DCO^+ exhibits a double peak, one near the ring's inner edge and the other in the outer disk. With complementary observations of lower-lying transitions, we constrained the molecular surface densities and rotation temperatures. We compared the derived quantities with model predictions across different cosmic-ray ionization (CRI) rates, carbon-to-oxygen (C/O) ratios, and stellar UV fluxes. Cold molecular chemistry, affecting the N_2H^+, DCO^+, and H_2D^+ abundances, is most sensitive to the CRI rate, while the stellar UV fluxes and C/O ratios have minimal impact on these three ions. Our best model requires a low CRI rate of 10^{-18} s^{-1}. However, it fails to match the low temperatures derived from N_2H^+ and DCO^+, 12–16 K, which are much lower than the CO freezing temperature.

Unified Astronomy Thesaurus concepts: Protoplanetary disks (1300); Planet formation (1241); Astrochemistry (75); Isotopic abundances (867)

1. Introduction

A protoplanetary disk is a crucial stage in the evolution of cosmic matter, where the interplay of inherited material from a parent cloud and the in situ physics and chemistry establishes the conditions for planet formation. Protoplanetary disks are characterized by complex chemical stratification owing to radial and vertical variations in density, temperature, ionization, and dissociative radiation (Y. Aikawa et al. 2002). The uppermost layers usually allow the formation of simple atoms, ions, and photo-stable radicals, while the intermediate warm molecular layer produces most of the gas-phase molecules traced by Atacama Large Millimeter/submillimeter Array (ALMA) observations. There is minimal penetration of stellar radiation in the innermost regions near the midplane in the vertical direction, making them very cold and poorly ionized. In this dense region, most of the molecules freeze onto grain surfaces. Hence, midplane regions are very difficult to probe. N_2H^+, DCO^+, and H_2D^+ are among the very few molecules which remain in the gas phase in the midplane region (C. Ceccarelli et al. 2004; K. I. Öberg et al. 2011).

N_2H^+ is expected to be abundant in regions where CO is depleted. This anticorrelation is observed in both dense cores (e.g., P. Caselli et al. 1999; E. A. Bergin et al. 2002) as well as in disks (C. Walsh et al. 2012). N_2H^+ is produced through the protonation of N_2 and rapidly destroyed by CO to form HCO^+.

Table 1
Spectral Setup of the ALMA Band 7 Observations of GG Tau A

Spectral Window	Central Frequency (GHz)	Bandwidth		Resolution		No. of Channels
		Frequency (MHz)	Velocity (km s^{-1})	Frequency (MHz)	Velocity (km s^{-1})	
25	358.000000	1875.00	1570.2	1.129	0.945	3840
27	359.770685	117.19	97.7	0.141	0.118	1920
29	360.169780	117.19	97.5	0.141	0.117	1920
31	369.908554	117.19	95.0	0.141	0.114	1920
33	372.421385	117.19	94.3	0.122	0.098	1920
35	372.672493	58.59	47.1	0.141	0.114	960

Hence, N_2H^+ can persist in the gas phase at temperatures a few kelvin below the CO freeze-out temperature (K. I. Öberg et al. 2005). N_2H^+ has been observed in multiple disks (e.g., A. Dutrey et al. 2007; C. Qi et al. 2013; N. T. Phuong et al. 2021; D. E. Anderson et al. 2022), but is often characterized by comparatively weak emission.

An enhanced abundance of H_2D^+ is predicted by chemical models at low temperatures ($T < 20$ K), with the major formation pathway being protonation of HD (H. Roberts & T. J. Millar 2000). H_2D^+ can only be observed in high-density regions with low CO and N_2 content where H_3^+ has not already been destroyed. H_2D^+ has already been detected in prestellar cores (e.g., P. Caselli et al. 2008), but there is no clear detection in any of the protoplanetary disks (e.g., C. Ceccarelli et al. 2004; W. F. Thi et al. 2004; C. Qi et al. 2008; E. Chapillon et al. 2011).

DCO^+ serves as an effective indicator of low-temperature CO freeze-out regions within the disk and is predominantly formed through the interaction of CO with H_2D^+ (A. Wootten 1987). On the one hand, the formation of H_2D^+ mainly occurs through HD protonation and is hindered by the destruction of H_3^+ in the presence of CO. On the other hand, the presence of CO is essential for DCO^+ formation. Consequently, DCO^+ emission is expected to peak in a narrow region around the CO snow line where both the parent molecules are in the gas phase in small amounts (Y. Aikawa et al. 2002; K. Willacy 2007; G. S. Mathews et al. 2013).

In summary, N_2H^+, DCO^+, and H_2D^+ are excellent tracers of low-temperature, high-density regions of the disk, specifically the midplane region in outer disks. Simultaneous observations of these molecules allow us to locate the CO snow line. Snow lines are thought to play an important role in planet formation because the ice coating on grains increases the solid mass, potentially promotes the coagulation of grains into larger particles, and/or the larger bodies formed from these grains require a higher collision velocity for destruction. These effects are particularly prominent just outside the snow line (S. Okuzumi et al. 2012). Additionally, such observations provide insights into ionization fractions within the relevant disk areas, offering constraints that can impact magneto-rotational instability. In instances of excessively low ionization fractions, "dead zones" (C. F. Gammie 1996) form, which are conducive to efficient grain growth and subsequent planet formation (e.g., K. I. Öberg et al. 2011).

This work reports spatially resolved emission from N_2H^+ (4–3) and DCO^+ (5–4) and upper limits for o–H_2D^+ (1(1, 0)–1(1, 1)), ^{13}CS (8–7), and SO_2 19(4, 16)–19(3, 17) in the disk around a triple stellar T Tauri system, GG Tau A, utilizing the ALMA interferometer. This represents the most sensitive observation of these molecules in GG Tau A to date. The system (age 1–5 Myr) is located at a distance of 150 pc (using the Gaia parallax measurements of the GG Tau Ba star of this hierarchical quintuple system, because those of GG Tau A are contaminated by its triple nature; Gaia Collaboration et al. 2016, 2018) from us in the Taurus–Auriga star-forming region. This circumtertiary disk is characterized by a dense ring of gas and dust between 193 and 285 au (from here on, we simply use the term "ring" to denote this region) where 90% of the continuum emission arises and an outer disk extended up to 800 au in ^{13}CO observations (S. Guilloteau et al. 1999; A. Dutrey et al. 2014). The majority of the total disk mass (0.15 $M_\odot$) is concentrated in the ring region (0.13 $M_\odot$; S. Guilloteau et al. 1999; S. M. Andrews et al. 2014). A. Dutrey et al. (2014) reported the presence of a hot spot located at the outer edge of the dense ring where a partial CO gap is observed (Y.-W. Tang et al. 2016), suggesting the presence of an embedded planet. This hypothesis is reinforced by the detection of a CO spiral emanating from the hot spot (N. T. Phuong et al. 2020a).

This disk is very cold, with a midplane temperature of ~14 K (A. Dutrey et al. 2014) and an atmospheric temperature of ~30 K (S. Guilloteau et al. 1999; N. T. Phuong et al. 2020b), at a radial distance of 214 au from the center. The first ever detection of H_2S in the outer disk of GG Tau A by N. T. Phuong et al. (2018) further confirms how dense and massive this system is. Given its substantial mass, high density (which should ease the detection of weak molecular lines), and low temperature, GG Tau A emerges as an ideal candidate for unraveling the intricacies of cold molecular chemistry within a protoplanetary disk.

We present our observational details in Section 2 of this paper. We explain the schemes we undertake to reduce the data in Section 2.1 and the observational results in Section 2.2, including integrated intensity maps, radial profiles, and Keplerian deprojected spectra. We also constrain the surface density of the detected molecules and the upper limits of surface density for the undetected molecules, as explained in Section 3. We perform a chemical analysis to understand our observations better using our astrochemical model, detailed in Section 4. We discuss our results in Section 5 and summarize the key understandings of our study in Section 6.

2. Observations

The GG Tau A system (International Celestial Reference System 04:32:30.3460, 17:31:40.642) was observed as part of the ALMA project #2021.1.00342.S (PI: Liton Majumdar) targeting to investigate the presence of Band 7 transitions, o–H_2D^+ (1(1, 0)–1(1, 1)), N_2H^+ (4–3), DCO^+ (5–4), ^{13}CS (8–7), and SO_2 19(4, 16)–19(3, 17). The observations were made over two executions using 47 antennas with baselines ranging from 14 to 456 m for a total on-source integration time of 2.7 hr. The spectral setup details can be found in Table 1.

2.1. Data Reduction

Calibration procedures involved bandpass and flux calibration, with the quasar source J0423-0120 utilized for this purpose. Phase calibration was conducted using the sources J0510+1800 and J0440+1437. The observed data were initially calibrated with the Common Astronomy Software Applications (CASA) package (version 6.4.1.12) pipeline. Subsequently, five rounds of continuum self-phase calibration were performed for each execution, selecting line-free channels carefully. The self-calibration solutions were then applied to the entire data set. To determine the disk center, we fitted the continuum structure with an ellipse, and both executions were recentered to the disk center using the `fixvis` task in CASA. The offset between the disk centers in the two executions was only (0.″005, 0.″003), which is well below our observed angular resolution of 0.″5–0.″9. Data with identical spectral setups from both executions were then combined using the `concat` task in CASA. We performed continuum subtraction on the self-calibrated recentered data by fitting a first-order polynomial to the continuum channels using the `uvcontsub` task in CASA. We constructed the images from our visibility data set in the `tclean` task in CASA using the `hogbom` deconvolving algorithm with `briggs` weighting (robust = 1.0). This yielded an angular resolution of 0.″93 × 0.″77 at a position angle (PA) of 68.°76, and a typical sensitivity of 14.6 mJy beam^{-1} for N_2H^+ (channel maps are presented in Figure A1). For DCO^+, we achieved an angular resolution of 0.″91 × 0.″73 at a PA of 99.°20, with a sensitivity of 5.6 mJy beam^{-1} (channel maps are presented in Figure A2). For H_2D^+, the noise (16.7 mJy beam^{-1}) is higher as the atmospheric transmission is degraded at this high frequency. For the weaker lines, including H_2D^+, we have used the `multiscale` deconvolver with `scales = [0, 5, 15, 25] × pixels` where each pixel corresponds to one-seventh of the beam size. We adopted the `natural` weighting scheme to enhance the signal-to-noise ratio for the weak lines. The masks used during cleaning were generated with the `keplerian_mask.py` tool[16] with the geometric parameters $M_* = 1.37\ M_\odot$, $i = 37°$, and PA = 278° confined within inner and outer radii of 1″ and 3.″5, respectively (values rescaled from S. Guilloteau et al. 1999 for a distance of 150 pc). Additionally, a continuum image was generated for a spectral window with a central frequency of 358 GHz, utilizing the line-free channels. The deconvolution algorithm employed was `hogbom`, and the process utilized the `briggs` weighting scheme with the robust parameter set to 0.

2.2. Observational Results

The integrated intensity maps were generated by collapsing the image cubes along the velocity axis while applying the Keplerian masks used for cleaning. We did not use any intensity threshold criteria to decide the inclusion of pixels while generating the moment map. For this purpose, we employed `bettermoments` Python package (R. Teague & D. Foreman-Mackey 2018). Figure 1 displays integrated intensity maps for the targeted molecules, where the elliptical contours indicate the location of the dust continuum ring region (193–285 au) of the disk of GG Tau. It also displays the continuum image at the central frequency of 358 GHz in the bottom right corner. Clear detections of N_2H^+ (4–3) and DCO^+ (5–4) are observed, while o–H_2D^+ (1(1, 0)–1(1, 1)), ^{13}CS (8–7), and SO_2 19(4, 16)–19(3, 17) show no detection.

We generated the radial distributions of velocity-integrated intensity across the disk from the zeroth moment maps with the help of the `radial_profile` function in the `GoFish` Python package (R. Teague 2019) by dividing the disk radial range into a series of annular rings with a width of one-quarter of the beam major axis and averaging the emission for each ring. The radial profiles for N_2H^+ (4–3) and DCO^+ (5–4) are shown in Figure 2. The two vertical lines indicate the ring region (193–285 au). We have also shown the radial profiles for all the transitions generated without Keplerian masking in Figure A4. DCO^+ shows a slightly lower emission in the ring region in this case.

We employed the shifting and stacking technique using the `integrated_spectrum` function in the `GoFish` package (R. Teague 2019) to generate a disk-integrated spectrum. Velocities for each pixel were shifted to the systemic one, 6.4 km s^{-1}, utilizing the system's kinematic information used in the generation of the Keplerian mask and stacked to create a Keplerian deprojected spectrum for each transition. The radial range for generating the integrated spectrum is between 120 and 550 au. We have done a Gaussian fit to the observed spectrum using `scipy.optimize.curve_fit` to determine the peak intensity and the velocity at which the peak occurs. The width of the observed signal is the FWHM, given by $2\sqrt{2\ln 2}\,\sigma$, where σ is the standard deviation calculated from our fit. We used the `numpy.trapz` function to calculate the disk-integrated flux density of the line signal over a velocity range determined by visual inspection (the shaded region in Figure 3). The Keplerian deprojected spectra are shown in Figure 3. The stacked spectra for N_2H^+ (4–3) and DCO^+ (5–4) are peaking at the systemic velocity, v_{LSRK} of 6.4 km s^{-1}, confirming the detections. The disk-integrated flux densities are reported in Table 2. The 1σ errors are calculated as $f \times \delta S \times \delta v \times \sqrt{N}$, where f is the spectral correlation factor derived from the noise autocorrelation spectrum, δS is the noise associated with each channel, δv is the channel width, and N is the number of channels over which the integration is performed.

We further verified our detections with the matched filtering technique (R. A. Loomis et al. 2018a). In this method, we cross correlate the observed visibility with the modeled visibility derived from the Keplerian masks used during cleaning. We utilized a package called `VISIBLE` (R. A. Loomis et al. 2018b) for this task. For N_2H^+ (4–3), we found a filter response of 43σ, and for DCO^+ (5–4), it is 20σ at the systemic velocity of 6.4 km s^{-1} (Table 2). The matched filter responses are shown in Figure A5.

Additionally, calibrated visibilities were exported to UVFITS format using the CASA task `exportuvfits` for subsequent analysis with the IMAGER program[17] and the DISKFIT disk model fitting tool (V. Piétu et al. 2007). Spectra and radial peak brightness profiles generated by `KEPLER` are presented in Figure B1 in Appendix B. The `KEPLER` command in IMAGER is similar to the `GoFish` package. The reconstructed spectra and radial profiles slightly differ from those in Figure 3 because of the higher angular resolution (0.″65 × 0.″53 at a PA of 80°) used in IMAGER.

Both N_2H^+ (4–3) and DCO^+ (5–4) are detected with a very high signal-to-noise ratio, with N_2H^+ (4–3) being the stronger detection among the two. Radial profiles (Figures 2 and B1)

[16] https://github.com/richteague/keplerian_mask

[17] https://imager.oasu.u-bordeaux.fr

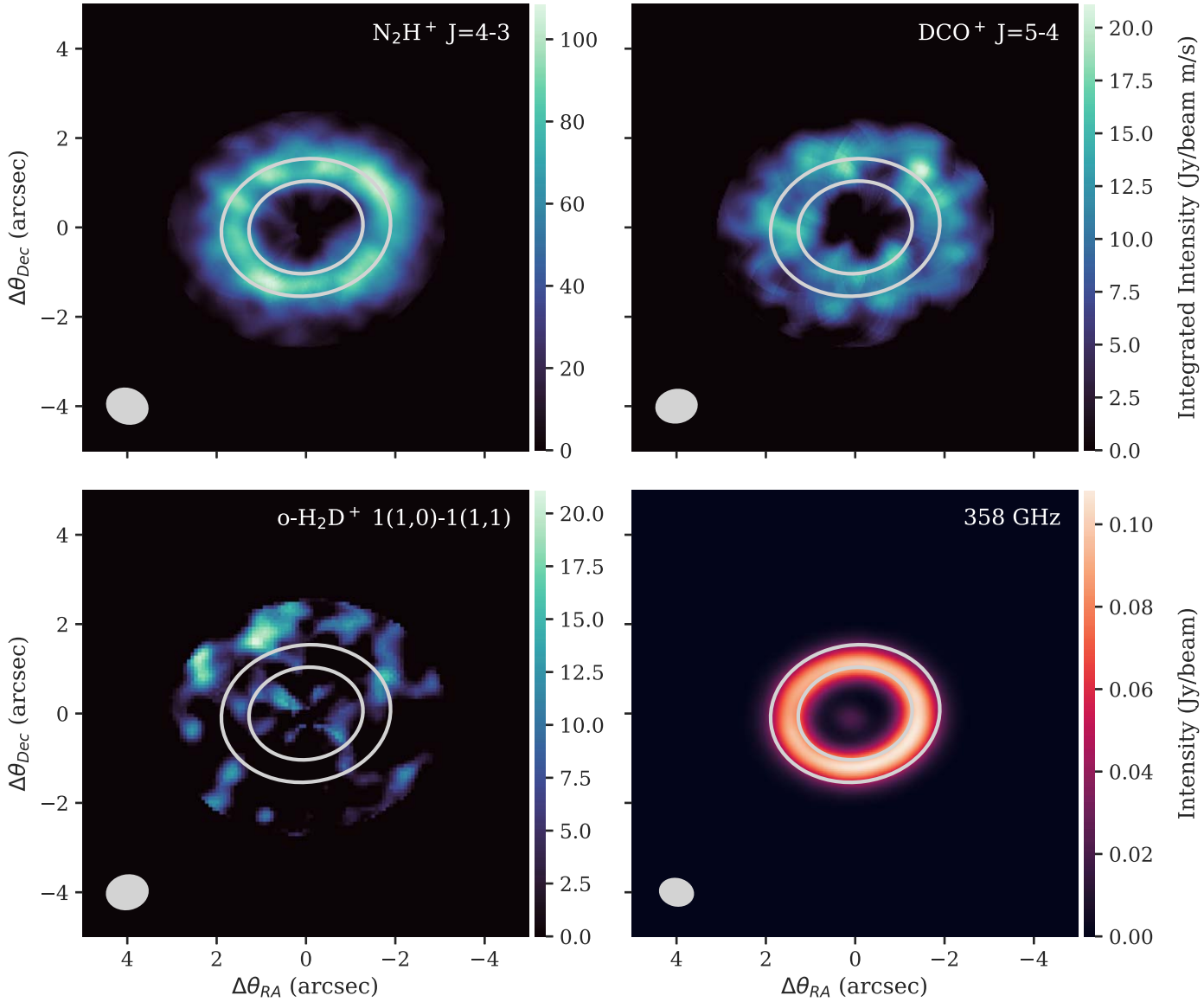

Figure 1. Integrated intensity maps of the targeted lines N_2H^+ (4–3), DCO^+ (5–4), and o–H_2D^+ (1(1, 0)–1(1, 1)). The overplotted elliptical ring contours in white are at 193 au (1.″28) and 285 au (1.″9) to indicate the continuum ring region. Both N_2H^+ and DCO^+ emissions are extended beyond the ring region. As far as H_2D^+ is concerned, there is no significant emission from the ring region. The figure at the lower right corner is the continuum image at 358 GHz.

indicate that the N_2H^+ (4–3) emission exhibits a ring-like radial distribution, peaking near the outer edge of the continuum ring. In contrast, the radial distribution of the DCO^+ (5–4) peak brightness temperature (Figure B1) shows a double-ringed structure. The inner DCO^+ (5–4) emission arises from the continuum ring, while an outer, brighter DCO^+ (5–4) emission originates from the outer disk region. This suggests radial variations in the deuteration process across the disk. However, this double-ringed structure is less prominent in the velocity-integrated radial profile (right panel in Figure 2), possibly due to the lower angular resolution. Other targeted species, including H_2D^+, ^{13}CS, and SO_2, are not detected (Figure A5).

3. Derivation of the Disk's Physical Parameters

3.1. DISKFIT Modeling

To derive disk properties, we perform a least squares fit to the observed visibilities to adjust an empirical parametric disk model to the data, using the DISKFIT tool from V. Piétu et al. (2007). This approach allows an accurate derivation of the geometrical parameters. Furthermore, when several transitions of the same molecules are available, it allows a quantitative estimate of the molecular surface densities and excitation temperatures. It also allows for consistent estimates of the errors on the disk parameters (within the framework of the adopted disk model). This can be done either from the covariance matrix (when parameter coupling is limited) or through a more elaborate Markov Chain Monte Carlo method.

The disk model is similar to that used in N. T. Phuong et al. (2020b). It uses a flared disk geometry with a Gaussian vertical profile and a radial power law for the scale height. Molecules are assumed to follow the same vertical distribution for simplicity. The model assumes level populations are governed by the Boltzmann law, with the temperature being a power law as a function of radius. For a simple comparison with the observed data, we assume that the intrinsic line width remains constant with radius. In fact, fitting line width as a power law instead suggests a small but not significant decrease of intrinsic

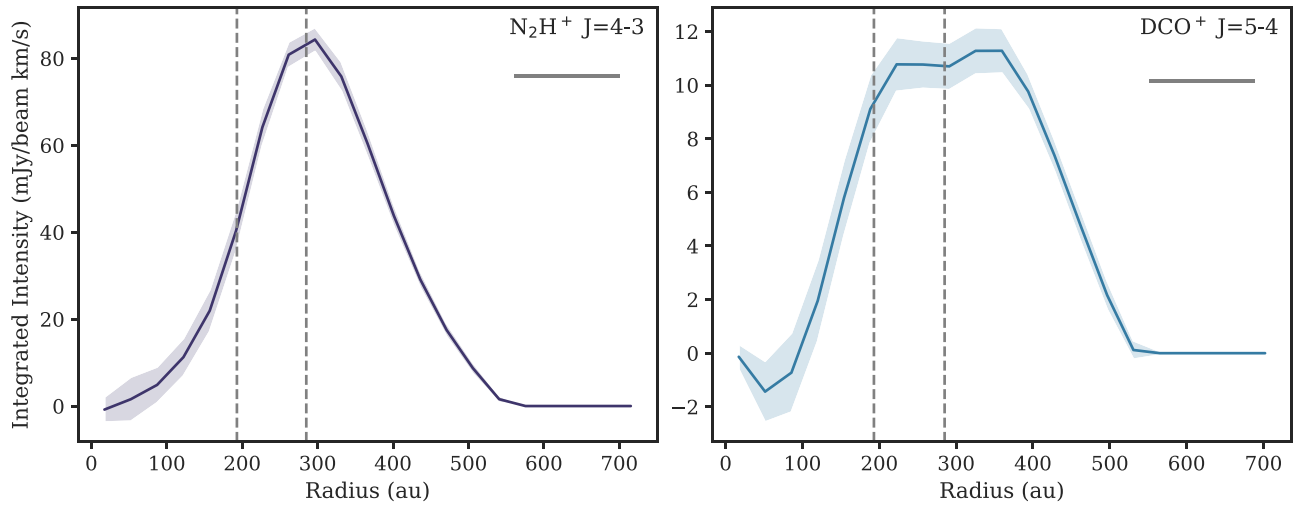

Figure 2. Azimuthally averaged velocity-integrated radial profiles of the detected lines generated from the integrated intensity maps shown in Figure 1. The shaded region in the above figure corresponds to 1σ. The dashed vertical lines are to designate the location of the ring around GG Tau A, spanning from 193 to 285 au. The gray horizontal line at the top right corner represents the beam major axis.

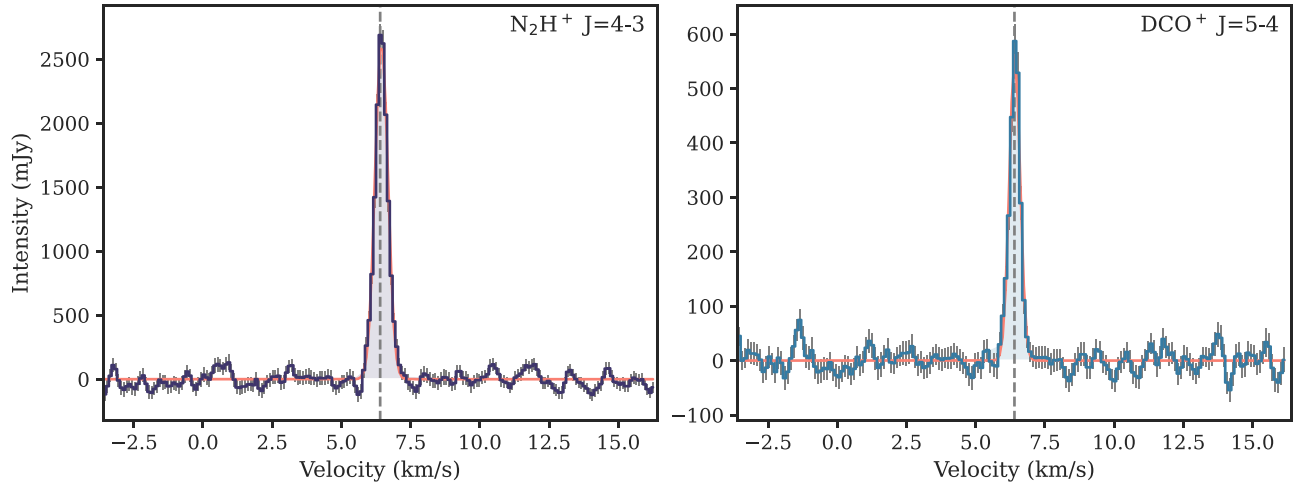

Figure 3. Keplerian deprojected and stacked spectra of the detected lines N_2H^+ (4–3) and DCO^+ (5–4). The shaded region is the region over which we have done a Gaussian fitting (orange curve) and calculated the integrated flux densities. The stacked spectra are peaking at the systemic velocity, v_{LSRK} of 6.4 km s^{-1}, confirming the detections. The location of the systemic velocity is shown by the vertical dashed lines. Integrated flux densities and matched filter responses are tabulated in Table 2.

Table 2
Properties of the Lines Observed

Species	Transition	Frequency (GHz)	E_u (K)	$\log_{10}(A_{ul})$ (s^{-1})	g_u	Filter Response (σ)	Integrated Intensity (mJy km s^{-1})	Line Width (km s^{-1})
N_2H^+	4–3	372.6724808	44.71	−2.50934	81	43	1570 ± 40	0.55 ± 0.01
DCO^+	5–4	360.1697783	51.86	−2.42480	11	20	290 ± 20	0.46 ± 0.01
H_2D^+	1(1, 0)–1(1, 1)	372.4213558	104.20	−3.96567	9	⋯	<58	⋯
^{13}CS	8–7	369.9085505	79.89	−2.97351	34	⋯	<70	⋯
SO_2	19(4, 16)–19(3, 17)	359.7706846	214.26	−3.41473	39	⋯	<35	⋯

Note. Here, E_u is the upper energy level of the transition, A_{ul} is the Einstein coefficient for spontaneous transition, and g_u is the upper state degeneracy. The error bars on the integrated intensity for the detected molecules are 1σ. We have calculated a 3σ upper limit on flux densities for the undetected molecules for an integration area between radii of 150 and 450 au and a line width of 0.55 km s^{-1} (Appendix C). The line width comes from the FWHM of the Gaussian fitting in Figure 3 (Section 2.2).

line width with radius that does not affect the other disk parameters. The emerging line intensity is derived using simple ray tracing, considering the geometry and dynamics (position, orientation, inclination, velocity, and Keplerian rotation pattern) and level populations computed at every sampled point along the line of sight. The hyperfine structure of the observed lines is also considered at this stage. This approach implicitly accounts for line optical depth. Visibilities are then computed on the same (u, v) points as the data from the 3D data cube. A least squares minimization is performed on the

Table 3
Geometric and Dynamic Parameters Determined through DISKFIT Modeling

Quantity	N_2H^+ (4–3)	DCO^+ (5–4)	Adopted
X_0 (arcsec)	-0.007 ± 0.011	0.019 ± 0.016	0
Y_0 (arcsec)	-0.001 ± 0.007	0.004 ± 0.011	0
PA (deg)	8.4 ± 0.5	8.1 ± 0.5	8
i (deg)	36.5 ± 0.4	37.0 ± 0.4	37
V_{sys} (km s^{-1})	6.45 ± 0.03	6.43 ± 0.03	6.43
V_{100} (km s^{-1})	3.61 ± 0.03	3.54 ± 0.03	3.55

Note. Best-fit geometric parameters from the observed visibilities. Offsets (X_0, Y_0) are from the ring center. V_{100} is the Keplerian velocity at 100 au. A PA of 8° in DISKFIT is equivalent to 278° in GoFish. In DISKFIT, the PA is measured with respect to the disk minor axis, while in GoFish, this angle is measured with respect to the disk major axis. The "Adopted" column indicates the fixed parameter values used for the multitransition model fit in Table 4.

Table 4
Best-fit Parameters for the Molecular Distributions and Excitation Conditions

Quantity	N_2H^+	DCO^+	Units
δV	0.149 ± 0.005	0.150 ± 0.005	km s^{-1}
T_{250}	12.2 ± 0.7	16.0 ± 1.2	K
q	-0.32 ± 0.19	0.39 ± 0.15	…
N_1	22 ± 8	2.8 ± 0.6	10^{11} cm^{-2}
R_1	252 ± 9	210 ± 50	au
W_1	95 ± 115	90 ± 360	au
N_2	12 ± 2	5.3 ± 1.0	10^{11} cm^{-2}
R_2	336 ± 20	375 ± 10	au
W_2	145 ± 15	90 ± 15	au

Note. Parameters derived from the best fit of a double Gaussian radial distribution model. N_i is the peak surface density of Gaussian distribution i, R_i is its peak position, and W_i is its width (FWHM). δV is the $1/e$ line width. T_{250} is the temperature at 250 au and q is the exponent of the temperature power law (a positive exponent indicates a quantity decreasing with radius).

different visibilities using a modified Levenberg–Marquardt algorithm. Guided by the radial distribution of velocity-integrated brightness (Figure 2) and apparent brightness temperature (Figure B1), we represented the radial surface density profiles for each molecule by the sum of two Gaussians, truncated to inner and outer radii of 150 and 550 au, respectively. The rotation temperature is assumed to be a simple power law, defined by its value at 250 au, T_{250}, and exponent q. The model thus has 15 possible parameters, six due to geometry and nine to represent the molecular distribution and excitation conditions (see Tables 3–4 for their designation).

Error bars are derived from the covariance matrix. The six geometric parameters, the line width δV, and temperature parameters exhibit very little coupling among them and with the other ones. However, the Gaussian distribution parameters are strongly coupled, particularly the pair (N_i, W_i) for distribution i, so their error bars should be treated with caution.

The parameter fitting process involves a two-stage approach. In the first stage, the geometric parameters are individually fitted for every observed transition. The geometric parameters derived from N_2H^+ and DCO^+ are given in Table 3, using the distance of 150 pc determined from Gaia. These transitions are relatively optically thin and, thus, more reliable tracers of the disk inclination than those previously used. Derived inclinations and orientation agree (but offer better precision) with previous determinations from CO isotopologues (A. Dutrey et al. 2014; N. T. Phuong et al. 2018).

The second stage entails averaging the corresponding values of the six geometric parameters across both spectral lines, fixing these averaged values, and proceeding to fit the remaining nine parameters.

To derive the surface densities and rotation temperatures, we used complementary data, which are made of the interferometric visibilities obtained with NOEMA for N_2H^+ (1–0) and DCO^+ (1–0) from N. T. Phuong et al. (2021), and DCO^+ (3–2) from N. T. Phuong et al. (2018). Geometric parameters from the "Adopted" column of Table 3 were used at this stage. Results are presented in Table 4. Figure 4 shows the constrained radial distributions of the surface densities. Agreement with the observations can be seen in Figure B1, where the best-fit radial profile (reconstructed by imaging the model visibilities and applying the Kepler deprojection) is compared with the data.

While this process is appropriate for DCO^+, the N_2H^+ distribution can almost equally well be represented by a single Gaussian or a truncated power law. This, however, does not affect the temperature derivation. The temperature that best represents N_2H^+ is almost constant, slightly increasing with radius, and quite low: 12 K. On the contrary, DCO^+ is better represented by higher temperatures, decreasing with radius from ∼18 K at 200 au to ∼12 K at 500 au.

As expected, the FWHM line width derived from the *uv* plane analysis with DISKFIT (0.25 km s^{-1} using the $1/e$ values in Table 4) is smaller than those in the recentered spectra from GoFish (0.55 km s^{-1}, Figure 3) and KEPLER (0.37 km s^{-1}, Figure B1) because of the remaining Keplerian shear within the synthesized beams used in these image plane reconstructions.

For H_2D^+, we simply assumed the same geometrical parameters ("Adopted" column in Table 3), a constant temperature of 15 K, and a uniform surface density between 150 and 450 au. The best-fit surface density of o–H_2D^+ from DISKFIT is then $(0.7 \pm 0.7) \times 10^{10}$ cm^{-2}. This gives the 3σ upper limit on o–H_2D^+ to be 2.1×10^{10} cm^{-2}.

3.2. Results

Figure 4 displays the radial distributions derived from the DISKFIT modeling. The results from a classical local thermodynamic equilibrium approach on the disk-averaged quantities (presented in Appendix C) are also indicated. The discrepancy between the radial profile and disk-averaged value for DCO^+ at large radii can be attributed to the assumption of constant $T_{rot} = 16$ K while the DISKFIT model shows it drops to 12 K at 500 au, leading to a stronger Boltzmann distribution correction factor.

We did not detect the lines o–H_2D^+ (1(1, 0)–1(1, 1)), ^{13}CS (8–7), and SO_2 19(4, 16)–19(3, 17). We calculated upper limits on the disk-averaged surface densities for these molecules using Equation (C3), while assuming optically thin emission. The calculations considered 3σ values integrated over the line width of N_2H^+ (coming from the Gaussian fit in Figure 3). Here, the noise $\sigma = f \times \delta S \times \sqrt{\delta v \times \Delta v}$, where f is the spectral correlation factor of 1.6, δS is the rms noise in the flux, δv is the channel width, and Δv is the line width over which the noise is calculated. The excitation temperature was fixed at 15 K for this purpose. The integration area Ω is considered for a radial region ranging from 150 to 450 au. The constrained values are tabulated in Table 5.

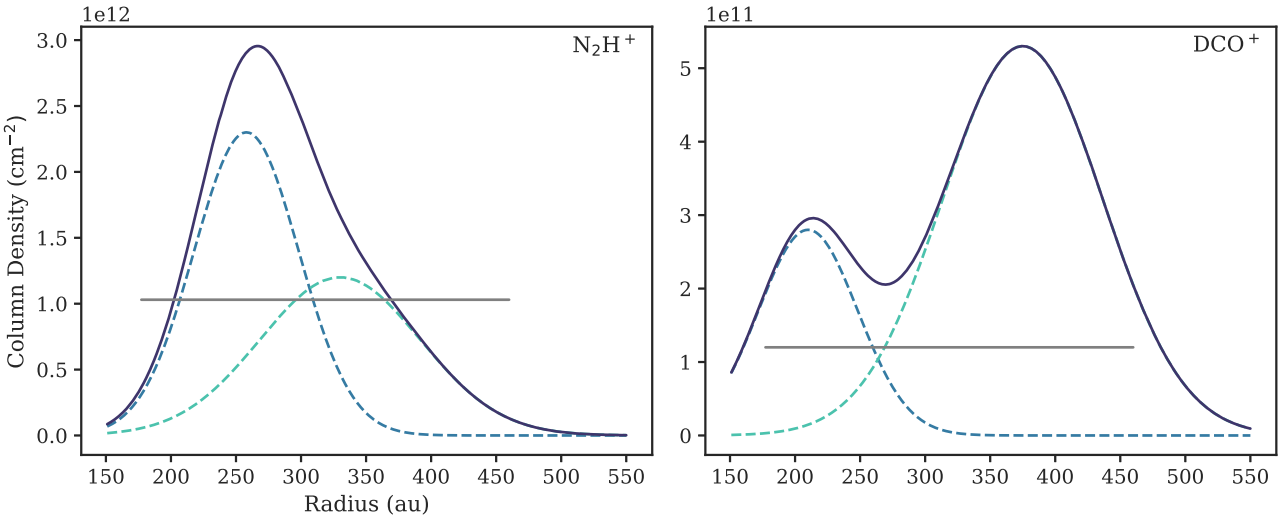

Figure 4. Radial distribution of the surface density derived from the DISKFIT modeling. The solid purple lines represent the total surface density while the dashed lines show the contribution from the individual Gaussians fitted in DISKFIT. The gray horizontal lines indicate the derived disk-averaged values using the simple LTE approach.

Our simple LTE approach reports an upper limit on the total (summation of both the ortho and para species) H_2D^+ surface density of 7.48×10^{12} cm^{-2}, while our DISKFIT analysis quotes an upper limit on the ortho–H_2D^+ surface density of 2.1×10^{10} cm^{-2}. Converting this to a total H_2D^+ surface density requires an assumption on the ortho-to-para ratio. Under the hypothesis of thermalization, this ratio can be very small since the ortho–H_2D^+ ground state is 86 K above the para ground state, leading to a huge Boltzmann correction factor (from 70 to 300 for temperatures ranging from 20 down to 15 K, respectively). At 15 K, the 3σ upper limit on the total H_2D^+ surface density, derived from the DISKFIT ortho–H_2D^+ value, is 6.3×10^{12} cm^{-2}.

Note that the low-level detection of ^{13}CS (2–1) with NOEMA, a low energy transition reported by N. T. Phuong et al. (2021), implies a surface density of 3×10^{11} cm^{-2} for $T_{\rm rot} = 15$ K, below our upper limit.

4. Astrochemical Modeling

4.1. Disk Physical Model

Our physical model is constructed for a radial range of 190–290 au, which primarily includes the ring region around the central stellar system GG Tau A. Only 10%–20% of the total disk mass is contained in the outer disk region, which, therefore, exhibits a lower density than in the ring. Moreover, the outer disk, under the shadow of the dense ring, is very cold (A. Dutrey et al. 2014; Y.-W. Tang et al. 2016; R. Brauer et al. 2019) with poor constraints on the physical properties. We chose not to focus our present modeling effort on this outer region, which has a more complex structure (Y.-W. Tang et al. 2016; N. T. Phuong et al. 2020b).

In the ring, the radial distribution of the midplane ($T_{\rm mid}$) and the atmospheric temperature ($T_{\rm atm}$) are taken as power laws, constrained in previous studies by A. Dutrey et al. (2014) and S. Guilloteau et al. (1999), respectively. They are of the form

$$T_{\rm mid}(r) = T_{{\rm mid},R_{\rm ref}} \left(\frac{r}{R_{\rm ref}}\right)^{-q}, \quad (1)$$

Table 5
Disk-averaged Surface Densities of the Detected Molecules and Upper Limits on the Undetected Molecules Under the Local Thermodynamic Equilibrium Assumption

Species	Transition	Surface Density, N_T (cm^{-2})	Excitation Temperature, T_{ex} (K)	Optical Depth, τ
N_2H^+	4–3	$(1.19 \pm 0.04) \times 10^{12}$	12 (fixed)	0.42
DCO^+	5–4	$(1.27 \pm 0.08) \times 10^{11}$	16 (fixed)	0.04
H_2D^+	1(1, 0)–1(1, 1)	$<7.48 \times 10^{12}$	15 (fixed)	⋯
^{13}CS	8–7	$<1.12 \times 10^{12}$	15 (fixed)	⋯
SO_2	19(4, 16)–19(3, 17)	$<2.46 \times 10^{16}$	15 (fixed)	⋯

Notes. (a) Surface density errors are coming from 16th and 84th percentiles of the posterior distribution. (b) The upper limits on the disk-averaged surface densities of the undetected molecules (H_2D^+, ^{13}CS, and SO_2) are constrained using the 3σ upper limit on the line flux as explained in Section C. (c) In this table, we have reported the upper limit on the total (sum of the ortho and para spin states) H_2D^+ surface density. The 3σ upper limit for o–H_2D^+ from the DISKFIT analysis is 2.1×10^{10} cm^{-2}.

$$T_{\rm atm}(r) = T_{{\rm atm},R_{\rm ref}} \left(\frac{r}{R_{\rm ref}}\right)^{-q}. \quad (2)$$

The values of the parameters can be found in Table 6. The radial dependency of the scale height, H_r at the disk midplane is calculated assuming hydrostatic equilibrium using the midplane temperature (Equation (1)), the mass of the stellar system, $M_* = 1.37\ M_\odot$ (rescaled from S. Guilloteau et al. 1999 considering a distance of 150 pc), the mean molecular weight of the gas per H nuclei $\mu = 2.37$, and the atomic mass unit, $m_{\rm H}$, as follows

$$\mathrm{H}_r = \sqrt{\frac{k_B T_{\rm mid}\, r^3}{\mu\, m_{\rm H}\, GM_*}}. \quad (3)$$

Here k_B and G are the Boltzmann and gravitational constants, respectively. We constructed the 1D vertical structure at each

Table 6
Parameter Prescription of the Best-fit Model Considered

Parameter Description	Values	Units
Fixed Parameters		
Stellar mass: M_*	1.37	$M_\odot$
Ring mass: M_g	0.13[a]	$M_\odot$
Ring inner radius: $R_{\rm in}$	193	au
Ring outer radius: $R_{\rm out}$	285	au
Reference radius: $R_{\rm ref}$	214	au
Midplane temperature at $R_{\rm ref}$: $T_{\rm mid,\ R_{ref}}$	14	K
Atmospheric temperature at $R_{\rm ref}$: $T_{\rm atm,\ R_{ref}}$	30	K
Surface density at $R_{\rm ref}$: $\Sigma_{g,\rm ref}$	9.7	g cm^{-2}
Temperature power-law index: q	1.1	
Temperature vertical gradient index: σ	0.5	
Surface density power-law index: γ	1.4	
Grain size: r_d	0.1	μm
Adjusted Parameters		
UV flux: $f_{\rm UV,R_{ref}}$	375	Draine's unit (χ_0)
Cosmic-ray ionization (CRI) rate, ζ_{CR}	10^{-18}	s^{-1}
Dust settling	Yes	
C/O ratio	1.0	
Age of the parent molecular cloud	10^6	yr
Age of the disk	10^6	yr

Note. All the fixed values, except σ and $\Sigma_{\rm ref}$, are taken from S. Guilloteau et al. (1999), A. Dutrey et al. (2014), and [a]S. M. Andrews et al. (2014) and rescaled considering a distance of 150 pc. σ is expected to be small as the inner edge of the ring casts a shadow on the rest of the structure (Y.-W. Tang et al. 2016). $\Sigma_{\rm ref}$ is calculated using Equation (5) assuming 0.13 $M_\odot$ of total disk mass is contained in the ring region.

radial point up to a 4 H_r height. The vertical temperature structure is adopted from E. Dartois et al. (2003) and J. P. Williams & W. M. J. Best (2014), which is given by

$$T(z) = T_{\rm mid} + (T_{\rm atm} - T_{\rm mid})\left[\sin\left(\frac{\pi z}{2z_q}\right)\right]^{2\sigma}. \quad (4)$$

$T_{\rm mid}$ and $T_{\rm atm}$ are defined at the midplane ($z = 0$) and the upper end ($z = z_q$) of the atmosphere assuming Equations (1) and (2), respectively. z_q is set at 4 H_r in our case. The parameter σ denotes the stiffness of the vertical temperature distribution. As pointed out by Y.-W. Tang et al. (2016), the inner edge of the GG Tau ring obstructs a substantial amount of starlight, minimizing the vertical temperature variation within. Therefore, we have chosen a value of 0.5 for σ. We have kept the dust temperature equal to the gas temperature, as dust and gas are relatively well coupled for such densities (>10^8 cm^{-3}).

The gas surface density, $\Sigma_g(r)$ [units of g cm^{-2}] is parameterized as a power-law profile suggested by D. Lynden-Bell & J. E. Pringle (1974), given by

$$\Sigma_g(r) = \Sigma_{g,R_{\rm ref}}\left(\frac{r}{R_{\rm ref}}\right)^{-\gamma}. \quad (5)$$

The power-law index γ is taken to be 1.4 following A. Dutrey et al. (2014). The gas surface density at the reference radius $R_{\rm ref}$, $\Sigma_{g,R_{\rm ref}}$ is calculated considering the mass contained in the circumtertiary ring, $M_g = 0.13\ M_\odot$ (S. Guilloteau et al. 1999; S. M. Andrews et al. 2014). The calculations are as follows

$$M_g = 2\pi\int_{R_{\rm in}}^{R_{\rm out}} \Sigma_g(r) r dr. \quad (6)$$

Substituting Equation (5) in Equation (6), for $R_{\rm ref} = 214$ au, we get

$$\Sigma_{g,R_{\rm ref}} = \frac{(2-\gamma)M_g}{2\pi R_{\rm ref}^{\gamma}}[R_{\rm out}^{2-\gamma} - R_{\rm in}^{2-\gamma}]^{-1} = 9.7\ {\rm g\ cm^{-2}}. \quad (7)$$

We then calculate the H_2 number density [units of cm^{-3}] at the midplane with

$$n_{\rm H_2,midplane} = \frac{\Sigma_g(r)}{\mu {\rm m_H} H_r\sqrt{2\pi}}. \quad (8)$$

Using the midplane density as the lower limit, we integrate the equation of hydrostatic equilibrium to obtain the vertical density structure (L. Reboussin et al. 2015)

$$\frac{\partial \ln n_{\rm H_2}(z)}{\partial z} = -\left[\left(\frac{GM_* z}{r^3}\right)\left(\frac{\mu m_{\rm H}}{k_B T}\right) + \frac{\partial \ln T}{\partial z}\right]. \quad (9)$$

The local visual extinction is determined from the hydrostatic density structure, assuming a conversion factor of $(A_v/{\rm N}_H)_0 = 6.25 \times 10^{-22}$ (R. Wagenblast & T. W. Hartquist 1989) where $N_{\rm H} = 2N_{\rm H_2}$ is the vertical hydrogen surface density. We assume $N_{\rm H}$, and consequently A_v, is zero above 4 H_r. To account for the impact of the grain size (r_d) and dust-to-gas mass ratio (ε), we scale the conversion factor as follows (V. Wakelam et al. 2019)

$$\frac{A_v}{N_{\rm H}} = \left(\frac{A_v}{N_{\rm H}}\right)_0 \frac{\varepsilon}{10^{-2}}\frac{10^{-5}}{r_d({\rm cm})}. \quad (10)$$

The stellar UV flux factor $f_{\rm UV}$ follows the inverse-squared law of distance and acts on the top of the disk atmosphere, only half of which is scattered toward the midplane, the rest being absorbed or scattered upwards (V. Wakelam et al. 2016)

$$f_{\rm UV}(r) = \frac{1}{2}\frac{f_{\rm UV,R_{ref}}}{\left(\frac{r}{R_{\rm ref}}\right)^2 + \left(\frac{4H_r}{R_{\rm ref}}\right)^2}. \quad (11)$$

$f_{\rm UV,R_{ref}}$ is defined at the surface of the disk in units of interstellar Draine field spectrum, χ_0 (B. T. Draine 1978) and reported in Table 6. H_r is calculated using Equation (3). The vertical distribution of UV flux is obtained by multiplying $f_{\rm UV}$ with $e^{-A_v/1.086}$, where A_V is the visual extinction distribution (F. Du & E. A. Bergin 2014).

In our models, we have not implemented grain growth; instead, we considered a uniform grain size of 0.1 μm (N. T. Phuong et al. 2018) settling below 1 H_r. To incorporate dust settling, we adjust ε to 10^{-3} above 1 H_r, while maintaining the standard value of ε of 10^{-2} below 1 H_r. Figure 5 illustrates the corresponding structure of the best physical model.

4.2. Chemical Model and Network

The gas–grain astrochemical model DNAUTILUS, introduced in L. Majumdar et al. (2017), is used to compute the 1 + 1D chemical composition in the ring of GG Tau A by incorporating all the updates from DNAUTILUS 2.0 outlined in K. Taniguchi et al. (2024). DNAUTILUS 2.0 has the capability to investigate deuterium fractionation in both two-phase (gas and grain surface) and three-phase (gas, grain surface, and grain bulk) modes. DNAUTILUS 2.0 includes 1606 gas species, 1472 grain-

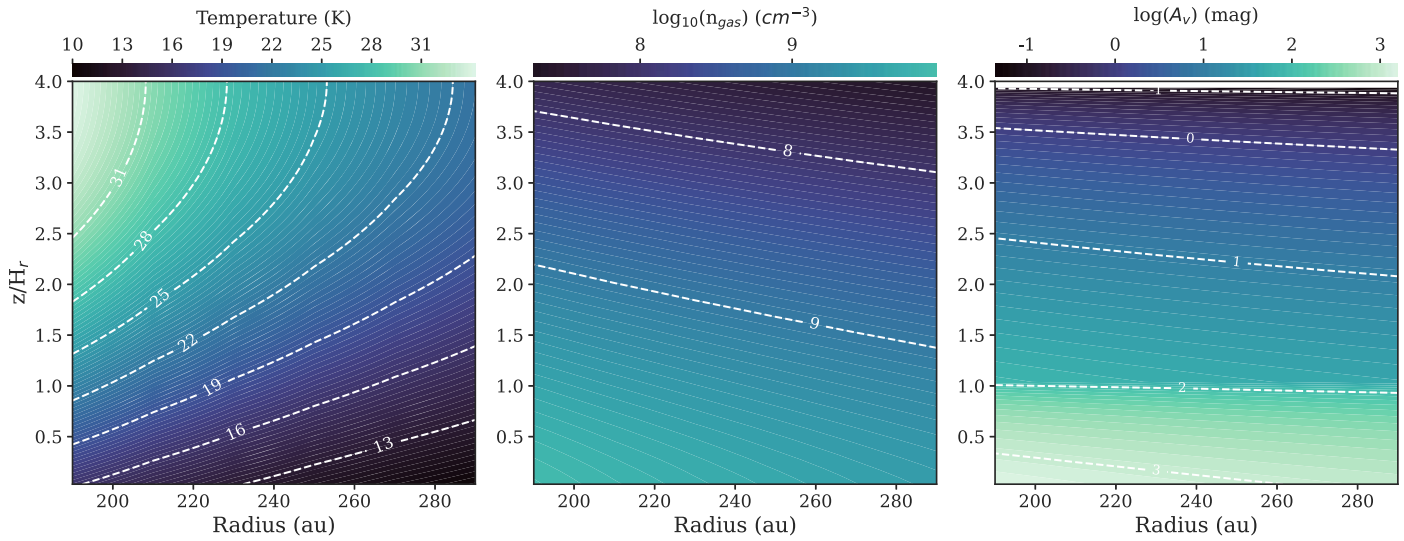

Figure 5. Physical structure of the ring region in our model derived using the parameters tabulated in Table 6. The left panel indicates the temperature distribution, the middle one is the gas density distribution in log scale, and the one on the right is the visual extinction in log scale. The description of the model is explained in Section 4.

surface species, and 1472 grain-mantle species, connected by 83,715 gas-phase reactions, 10,967 reactions on grain surfaces, and 9431 reactions in the grain mantles.

Although including spin-state chemistry of hydrogenated species like H_2, H_2^+, H_3^+, and their isotopologues would have allowed us to directly investigate o–H_2D^+ chemistry, we chose not to do so. The primary reason is that the newly proposed state-to-species and species-to-state reaction rates for the $H_3^+ + H_2$ systems by O. Sipilä et al. (2017) vary depending on density and temperature regimes. Applying them to a protoplanetary disk would require rigorous benchmarking and testing across various star-forming environments, and such extensive validation is beyond the scope of this paper.

4.3. Grid of Models

To find the model that best represents our observationally constrained radial surface density distributions of N_2H^+ and DCO^+, and the upper limits on H_2D^+, SO_2, and ^{13}CS (including the constraint from the $J = 2$–1 transition by N. T. Phuong et al. 2021), we explored a grid of models utilizing the least squares method (refer to Appendix D). These models span a range of initial carbon-to-oxygen (C/O) ratios, CRI rates, and UV flux values (see Table 8 in Appendix D). The model with the least disagreement with observations ($\chi^2_{\rm red} = 2.78$) is an inheritance disk model with initial abundances characterized from a starless dense molecular cloud, illuminated by stellar UV radiation of 375 χ_0 at a reference radius of 214 au. First, we allowed the molecular cloud to evolve chemically for 10^6 yr from initial atomic abundances (Table 7) with typical physical conditions such as a gas and dust temperature of 10 K, a total gas density of 2×10^4 cm^{-3}, a visual extinction of 15 mag, and a CRI rate of 1.3×10^{-17} s^{-1}. We then computed the temporal evolution of chemistry for the inherited material from the cloud in the ring region around GG Tau A for 10^6 yr. The assumption that protoplanetary disks form from a cold, starless, dense molecular cloud with the mentioned physical conditions is based on detailed discussions from V. Wakelam et al. (2019), without taking into account the chemical evolution between the cold core phase and the protoplanetary disk itself (M. N. Drozdovskaya et al. 2016).

Table 7
Initial Abundances Used in Our Cloud Model

Element	Abundance Relative to H	References
H_2	0.5	
He	9.00×10^{-2}	(1)
N	6.20×10^{-5}	(2)
O	$(1.40–3.3) \times 10^{-4a}$	(3)
C^+	1.70×10^{-4}	(2)
S^+	8.00×10^{-8}	(4)
Si^+	8.00×10^{-9}	(4)
Fe^+	3.00×10^{-9}	(4)
Na^+	2.00×10^{-9}	(4)
Mg^+	7.00×10^{-9}	(4)
P^+	2.00×10^{-10}	(4)
Cl^+	1.00×10^{-9}	(4)
F	6.68×10^{-9}	(5)
HD	1.60×10^{-5}	(6)

Note. (*a*) O initial abundance is adjusted for a C/O ratio ranging from 0.5 to 1.2.

References. (1) V. Wakelam & E. Herbst (2008); (2) E. B. Jenkins (2009); (3) L. Reboussin et al. (2015); (4) low metal abundances from T. E. Graedel et al. (1982); (5) depleted value from D. A. Neufeld et al. (2005); and (6) L. Majumdar et al. (2017).

It is crucial to highlight that in order to reproduce the observed surface densities in our disk simulation, a CRI rate ($\zeta_{\rm CR}$) of about 10^{-18} s^{-1} and an initial C/O ratio of 1.0 are necessary. Table 6 presents the parameters describing the best-fit model. Figure 6 showcases the modeled number density distributions within the ring region.

5. Discussion

5.1. Comparison with Previous Observations

o–H_2D^+ (1(1, 0)–1(1, 1)) has been observed in multiple dense starless cores and prestellar cores (see C. Ceccarelli et al. 2014 for a review). P. Caselli et al. (2008) report an o–H_2D^+ surface density $\sim 10^{12}$–10^{13} cm^{-2} in regions characterized by a gas density $\sim 10^5$–10^6 cm^{-3} and kinetic temperatures around

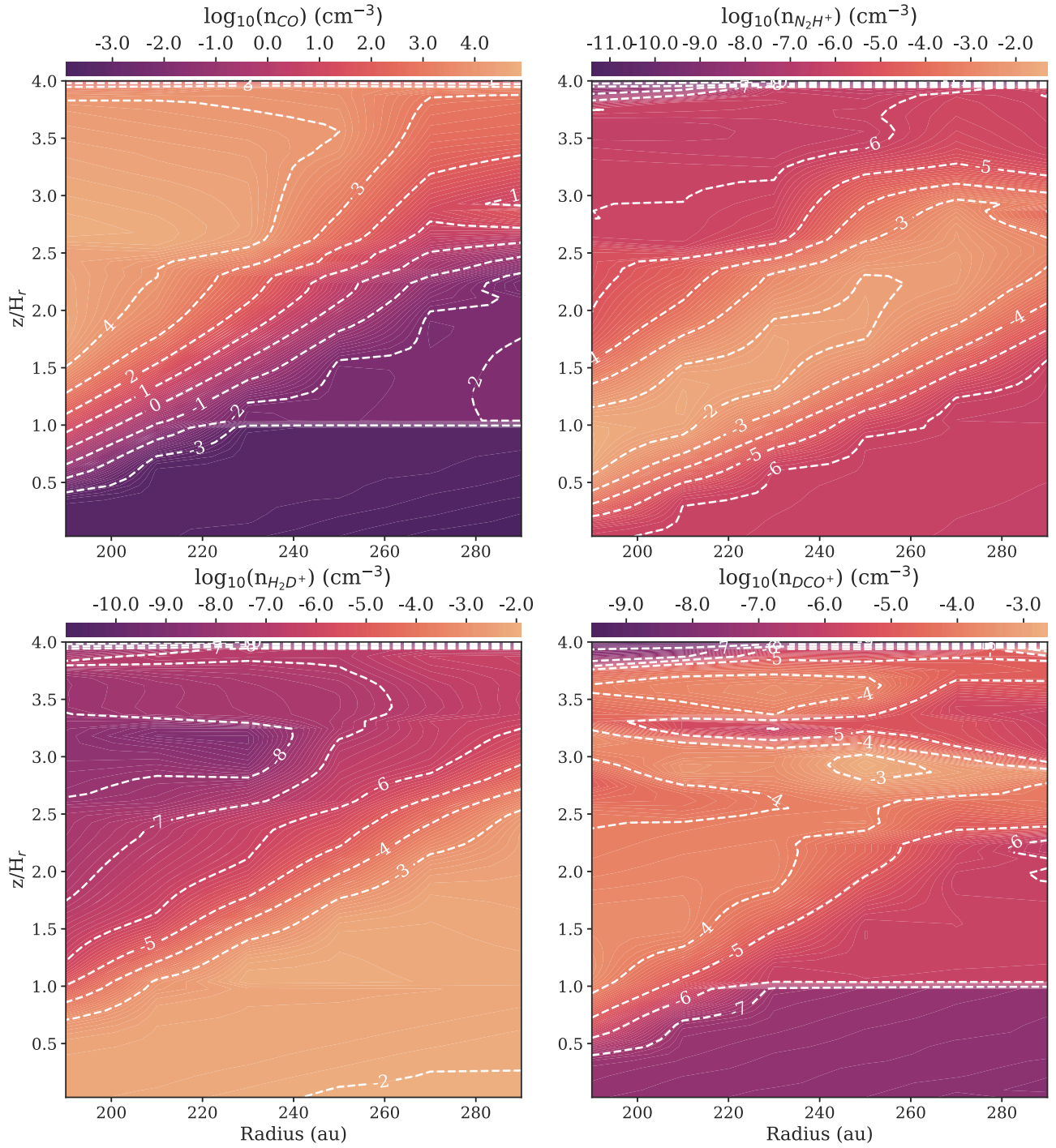

Figure 6. Number density distributions (log scale) from our best-fit model for CO, N_2H^+, H_2D^+, and DCO^+ from left to right and top to bottom. We have only modeled the ring region around GG Tau A, spanning a radial distance of 193–285 au from the central stellar system. The model disk atmosphere extends up to four scale heights.

10 K, with the most prominent detections in the densest and centrally concentrated cores. However, no clear detection has been obtained in protoplanetary disks. E. Chapillon et al. (2011) derived 3σ upper limits on the o–H_2D^+ surface density for the T Tauri disks DM Tau and TW Hya. Depending on the physical model, DM Tau's upper limit lies between 4.5×10^{11} and 1.9×10^{12} cm^{-2} and for TW Hya, it is between 9.0×10^{11} and 1.4×10^{12} cm^{-2}. Our upper limit for o–H_2D^+ in GG Tau is 2.1×10^{10} cm^{-2}. Note that E. Chapillon et al. (2011)'s upper limits are from single-dish observations (1σ noise level of 0.33 Jy km s^{-1}). We have achieved a much higher sensitivity (1σ noise level of 0.019 Jy km s^{-1}), making our observation the best available constraint on the upper limit of the o–H_2D^+ surface density in any disk to date.

The N_2H^+ (3–2) transition has been observed in five disks (three around T Tauri stars: IM Lup, GM Aur, and AS 209, and two around Herbig Ae stars: HD 163296 and MWC 480) as part of the Molecules with ALMA at Planet-forming Scales (MAPS) program (G. Cataldi et al. 2021). Despite the diverse continuum structures of the disks with multiple rings and gaps,

N_2H^+ emission showcases a ring morphology (Figure 4 in G. Cataldi et al. 2021). Our N_2H^+ emission is also characterized by a single-ring structure (Figure 2). C. Qi et al. (2013) have previously reported N_2H^+ detection toward TW Hya, and the single-ring emission structure is also evident there. The N_2H^+ ring morphology across different disks can be attributed to radial and vertical temperature variations (C. Qi et al. 2013). In the MAPS survey by G. Cataldi et al. (2021), two different N_2H^+ surface density values are derived by fixing the excitation temperature, T_{ex}, to (a) the observationally constrained CO freeze-out temperature, ∼20 K and (b) the midplane temperatures, T_{mid}, of the respective disks. For the T Tauri disks (IM Lup, GM Aur, and AS 209), the N_2H^+ surface density peaks around 10^{13} cm^{-2}, while for the Herbig Ae disks (HD 163296 and MWC 480), it reaches up to 10^{12} cm^{-2}. Interestingly, GG Tau, despite being a T Tauri disk, exhibits a N_2H^+ surface density of approximately 10^{12} cm^{-2}. The surface density in TW Hya reported by C. Qi et al. (2013) ranges from 4×10^{12} to 2×10^{15} cm^{-2} for different assumed physical structures. G. Cataldi et al. (2021) indicate that temperatures as low as 12 K in the N_2H^+-emitting region can also explain the observed flux of the 3–2 transition in the protoplanetary disks (e.g., GM Aur, HD 163296, and MWC 480) under the LTE assumption. Previously, in N. T. Phuong et al. (2021)'s study, N_2H^+ in GG Tau A was assumed to be arising from the same layer as CO, following a radial temperature variation, $T(r) = 20(r/250\ \mathrm{au})^{-1}$ K. Our direct measure of $T(r) = 12$ K for the N_2H^+-emitting region (Table 4), based on a multiline excitation analysis, suggests that we are tracing a region much closer to the midplane than initially assumed.

A ring-like radial distribution for DCO^+ has been commonly observed in multiple disks, including the TW Hya, DM Tau, AS 209, V4046 Sgr, MWC 480, and HD 163296 (C. Qi et al. 2008; G. S. Mathews et al. 2013; R. Teague et al. 2015; J. Huang et al. 2017) and is facilitated by reaction between H_2D^+ and CO (e.g., K. Willacy 2007). Contrary to the common scenario, we observe a partially overlapping double-ring radial distribution of DCO^+ emission in GG Tau A (refer to Figure 2), which can likely be attributed to different chemical effects in the ring and the outer disk regions owing to the difference in densities between the two regions. This is discussed in detail in Sections 5.2 and 5.3. Notably, K. I. Öberg et al. (2015) observe double DCO^+ rings in the disk IM Lup. They found that the DCO^+ abundance first decreases radially due to CO depletion, then another ring forms due to nonthermal desorption of CO in low surface density outer regions as a result of higher UV penetration. N. T. Phuong et al. (2018, 2021) have previously assumed that DCO^+ emission originates from the same region as N_2H^+ and CO, characterized by the radial temperature, $T(r) = 20(r/250\ \mathrm{au})^{-1}$ K in GG Tau A. In this work, we found that DCO^+ emission region is best represented by $T(r) = 16(r/250\ \mathrm{au})^{-0.39}$ K (Table 4). Hence, we expect that DCO^+ emission region lies vertically between the CO-emitting region and N_2H^+-emitting region and closer to the midplane than previously thought.

5.2. Chemical Trends in the Ring Region

We present a subset of chemical models for a selected set of input parameters in Figures 7 and 8 from the full model grids presented in Table 8. Only the CRI rates and the C/O ratios were found to have any significant impact on the modeled surface densities of the targeted molecules. Other parameters cannot be constrained by the current data.

CRI. Figure 7 shows the variation of the modeled abundances with CRI rate while keeping the C/O ratio constant at 0.7, and the remaining parameters are set to the best-fit values. The N_2H^+, DCO^+, and H_2D^+ abundances are quite sensitive to the CRI rate, while the UV flux values have no impact whatsoever. This is expected because these molecules probe a high-density, low-temperature, CO-depleted region near the midplane where UV penetration is minimal. Hence, cosmic rays are the primary ionization source for this cold molecular chemistry. However, the CRI rate has barely any impact on S-bearing species. It is worth noting that the standard interstellar CRI rate of 10^{-17} s^{-1} predicts an H_2D^+ surface density above the upper limit and a subinterstellar CRI rate of 10^{-18} s^{-1} explains the observationally constrained surface densities the best. This low CRI rate can be explained by a rise in the number of collisions experienced by cosmic-ray particles due to the greater effective surface density as they gyrate toward the disk midplane (M. Padovani et al. 2013). The attenuation is especially prominent in our case, as our chemistry focuses on high density near midplane regions. L. I. Cleeves et al. (2015) have previously inferred a very low CRI (10^{-19} s^{-1}) in the protoplanetary disk TW Hya, which they suggest is due to an exclusion by a young stellar wind. Our current astrochemical model only includes a constant CRI rate across the disk. The inclusion of short-lived radionuclides (L. I. Cleeves et al. 2013) and a vertical distribution of CRI rates (M. Padovani et al. 2018) may provide a better picture.

C/O ratio. We have also modeled the abundances of our targeted molecules for different elemental C/O ratios from 0.5 to 1.2 by changing the initial O abundances, as shown in Figure 8. Changing the C/O ratio from 0.5 to 1.0 decreases the N_2H^+ surface density by a factor of approximately 2.5, while the DCO^+ surface density increases by at most a factor of 1–2. However, when the C/O ratio was further increased to 1.2, changes in the surface densities of N_2H^+ and DCO^+ became significant (by a factor of approximately 10). The H_2D^+ surface density remains unaffected for any change in the C/O ratio from 0.5 to 1.2. The chemistry of ^{13}CS and SO_2, for which we obtained upper limits from our observations, is quite sensitive to changes in the C/O ratio. The general trend is that O-poor chemistry favors the formation of the C–S bond, and for SO_2, it is the other way around (see the discussions by D. Semenov et al. 2018; R. Le Gal et al. 2021, for further details). Our observations are best represented by a CRI rate of 10^{-18} s^{-1} and an elemental C/O ratio of 1.0. At the commencement of the evolution of a molecular cloud, a significant amount of important elements, including carbon and oxygen, exist in a refractory state, which is expected to shape the chemical budget of the protoplanetary disk formed from that cloud. Based on A. C. A. Boogert et al. (2015)'s observation of ice abundances, K. I. Öberg & E. A. Bergin (2021) report that about a 40% O chemical budget was unaccounted for at the onset of star and planet formation, leading to a poor constraint on the initial C and O gas-phase abundances. Our elemental C/O ratio of 1.0 suggests an oxygen-depleted environment in the dense ring. Similar inferences of high C/O ratios (0.9–2.0) were also found in more typical protoplanetary disks (e.g., R. Le Gal et al. 2021; M. Ruaud et al. 2022), which may have consequences on the formation of planets in the inner regions.

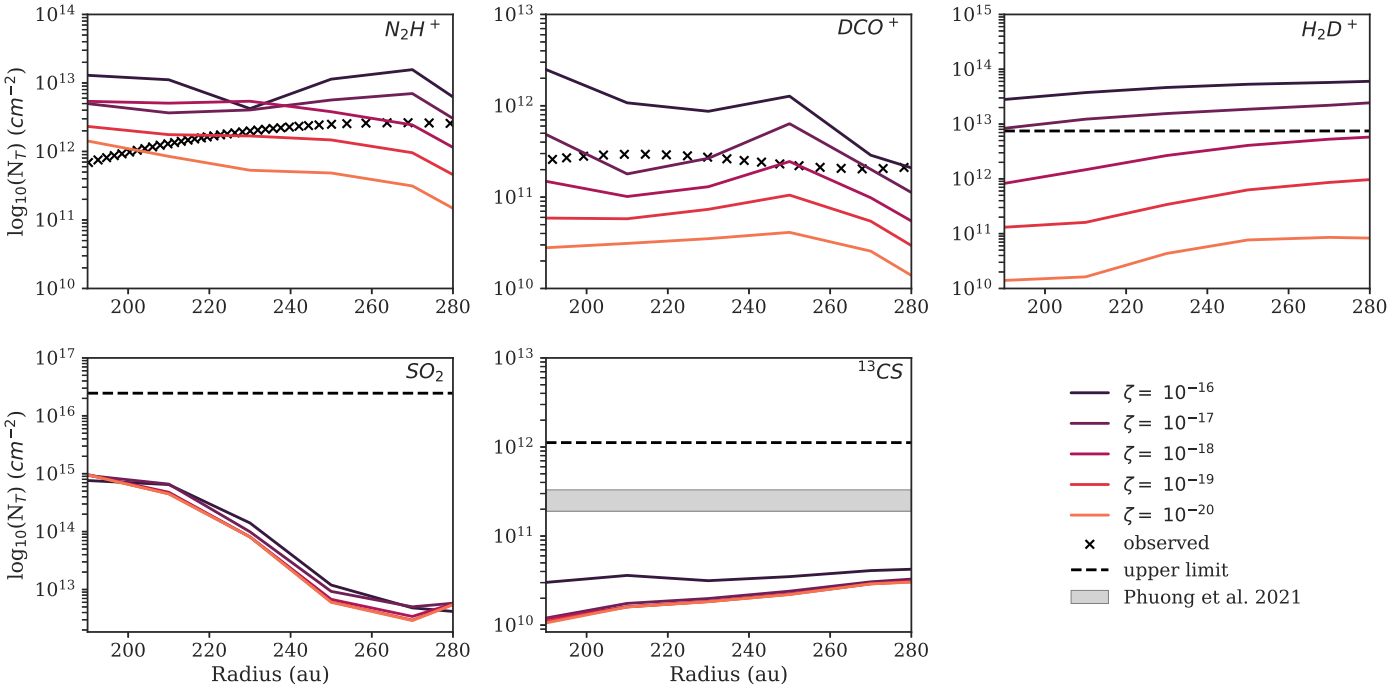

Figure 7. Comparison between models with different CRI rates (ζ) represented by the solid colored lines in the figure. Here, the "x" points represent the observationally contained surface density values from our DISKFIT analysis. The dashed horizontal lines represent observationally constrained upper limits on the surface density for the undetected molecules. The gray horizontal patch denotes the surface density constraint from a different transition of ^{13}CS ($J = 2$–1) by N. T. Phuong et al. (2021). Best model: CRI rate = 10^{-18} s^{-1} ($\chi^2_{\rm red} = 5.01$). Here, C/O = 0.7 and the rest of the parameters are set to the best-fit parameters. The upper limit on the ^{13}CS surface density is calculated from the CS surface density upper limit by assuming $N_{\rm CS}/N_{^{13}{\rm CS}} = 100$ (N. T. Phuong et al. 2021).

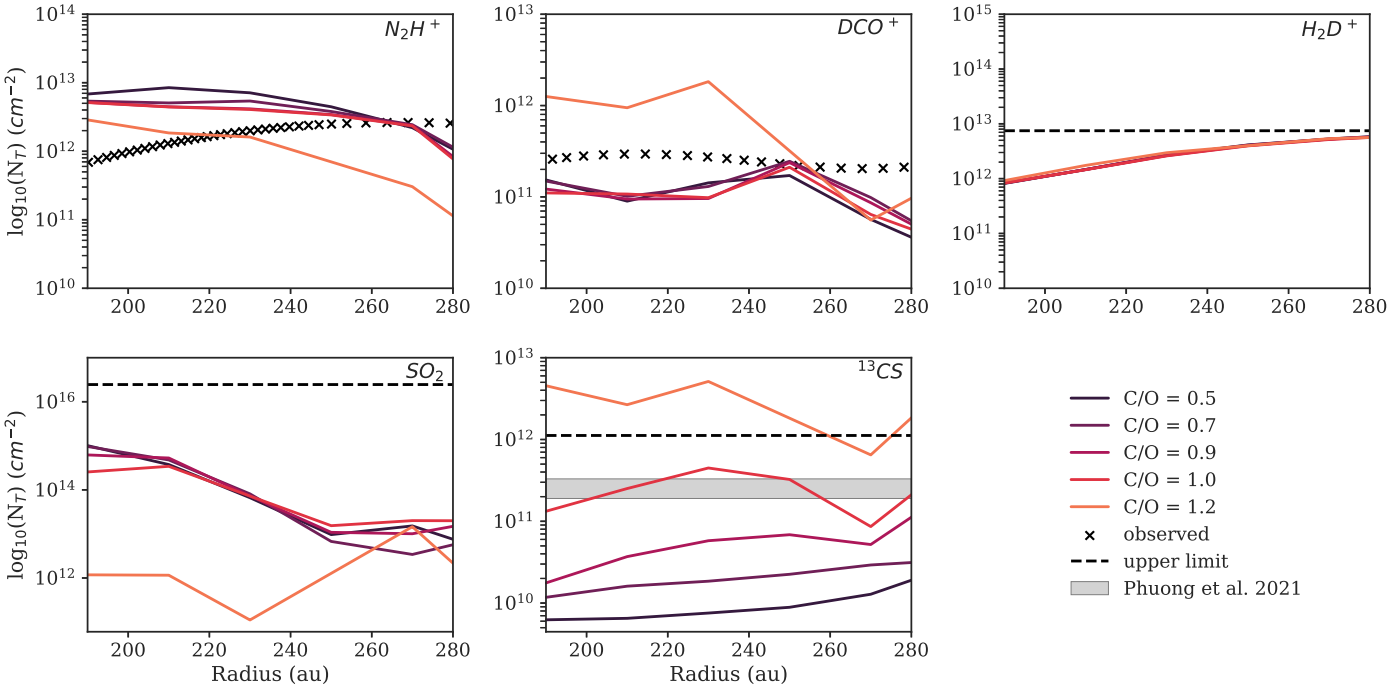

Figure 8. Comparison between models with different initial C/O ratios represented by the solid colored lines in the figure. The rest of the denotations are the same as Figure 7. Best model: C/O = 1.0 ($\chi^2_{\rm red} = 2.78$). All the parameters other than C/O are set to the best-fit parameters. The upper limit on the ^{13}CS surface density is calculated from the CS surface density upper limit by assuming $N_{\rm CS}/N_{^{13}{\rm CS}} = 100$ (N. T. Phuong et al. 2021).

Spatial distributions. Figure 6 represents the molecular number density distributions for our best model. We see a DCO^+ distribution in those regions where CO is available in the gas phase in small amounts. Observationally, DCO^+ follows a ring-like emission distribution in the ring region (refer to Figures 2 and B1). In our modeled abundances, DCO^+ is primarily peaking in temperature regions representative of the warm molecular layer (2.5–3.5 H_r), somewhat showcasing the ring-like distribution. One of the dominant ions in the warm molecular layer is HCO^+. It essentially forms through the protonation of CO and, in turn, produces DCO^+ through isotope exchange. The major reaction for DCO^+ production contributing to our observation above 2.5 H_r is

$HCO^+ + D \rightarrow DCO^+ + H$. We also see some DCO^+ arising below the warm molecular layer (~0.5–2.5 H_r) produced through a different channel, $CO + N_2D^+ \rightarrow N_2 + DCO^+$. Our DISKFIT analysis locates the peak of the DCO^+ ring at a radial distance of 210 ± 50 au (R_1 in Table 4), and this can be attributed to the fact that both DCO^+ formation channels are contributing to the DCO^+ abundances in this radial range. Near the disk midplane, DCO^+ starts depleting because its parent molecule, CO, efficiently freezes onto the grain surfaces owing to the high density and low temperature.

The N_2H^+ modeled distribution lies just below the DCO^+ layer, with its number density peaking in regions where DCO^+ starts depleting. Our observationally constrained representative temperatures of 16 and 12 K for the DCO^+- and N_2H^+-emitting regions, respectively (Table 4), suggest the same. N_2H^+ is abundant in the midplane at the inner edge of the ring as well as in the warm molecular layer (up to 3.0 H_r) at the outer edge of the ring. All throughout the ring region, the major formation pathway of N_2H^+ is the protonation of N_2, i.e., $N_2 + H_3^+ \rightarrow H_2 + N_2H^+$. So, the chemistry is mainly controlled by the gas-phase abundances of CO, N_2, HD, and H_3^+. As long as CO remains in the gas phase, it destroys N_2H^+ to form HCO^+. When CO starts depleting, N_2H^+ start increasing, as N_2 is still in the gas phase owing to its lower binding energy with respect to CO, forming N_2H^+, and there is less destruction of N_2H^+ because of the reduced CO presence. Our model predicts a decreasing N_2H^+ surface density with increasing radius, contrary to the observed increase within the continuum ring. This discrepancy arises primarily from the model's overestimation of N_2 depletion from the gas phase. A similar trend was observed in the protoplanetary disk around DM Tau, where V. Wakelam et al. (2019) conducted sensitivity analyses on various model parameters. One limitation of our model is the absence of a grain growth mechanism and the assumption that grains are perfectly spherical. A. Kataoka et al. (2013) proposed a dust growth mechanism in protoplanetary disks, which would create inhomogeneities in the dust distribution and potentially allow more UV penetration toward the disk's midplane. UV penetration, in turn, facilitates photodesorption of N_2. Chemically, nonspherical grains would have a larger cross-sectional area for collisions with gas-phase species and a larger surface area, increasing the likelihood of N_2 desorption. Additionally, our models do not include X-ray chemistry, which could also affect the abundance of N_2H^+ (L. I. Cleeves et al. 2015; R. Teague et al. 2015).

Our astrochemical model suggests that H_2D^+ is abundant in the midplane region, situated just below the N_2H^+ layer. The major formation pathway predicted by our model is $H_3^+ + HD \rightarrow H_2D^+ + H_2$. As N_2 begins to freeze onto grain surfaces, more H_3^+ become available for HD to capture, and we see a rise in H_2D^+ abundance and a fall in N_2H^+ abundance.

We did not detect H_2D^+. In our effort to replicate the observed surface density for the detected molecules, we realized that a lower CRI rate may provide the best explanation for our observations. H_2D^+ abundances are regulated by the availability of H_3^+, which in turn is dependent on the rate of ionization of H_2. A lower CRI rate results in reduced H_2^+ production ($H_2 + \text{cosmic ray} \rightarrow H_2^+ + e^-$), leading to a lower abundance of H_3^+ ($H_2 + H_2^+ \rightarrow H_3^+ + H$). Hence, a lower ionization rate at the midplane, owing to the very high density in the ring region, may explain the nondetection of o–H_2D^+ (1(1, 0)–1(1, 1)). Indeed, our model using a CRI rate (ζ_{CR}) of 10^{-18} s^{-1} predicts an H_2D^+ surface density of the order of $\sim 10^{12}$ cm^{-2} close to the current upper limit reported in Table 5. This limit suggests we are close to detection, and increasing the observation time should assure our chance of detection for H_2D^+. However, the upper limit on total H_2D^+ is based on the assumption of thermalized ortho-to-para ratio (LTE), with a high correction Boltzmann factor (see Section 3.2). While thermalization is facilitated by the very high midplane density, spin-dependent reaction rates may lead to a different prediction (e.g., E. Chapillon et al. 2011).

5.3. Possible Chemistry in the Outer Disk

N_2H^+ (4–3) and DCO^+ (5–4) emission is also spatially extended beyond the ring, reaching up to a radial distance of approximately 550 au (Figures 1, 2). The velocity-integrated radial profiles of N_2H^+ (4–3) and DCO^+ (5–4) (Figure 2) indicate that the former is decreasing as we go radially outward in the outer disk, while the latter shows another peak at around ~375 au.

We have not modeled the outer disk due to its complex structure (Y.-W. Tang et al. 2016; N. T. Phuong et al. 2020b). However, based on our current understanding, the outer disk is characterized by a lower density and colder temperatures as compared to the ring (refer to Section 4.1). Lower densities outside the dense ring allow higher cosmic-ray penetration, leading to nonthermal desorption of CO and N_2. Consequently, an increased presence of CO and N_2 in the gas phase is anticipated in the outer disk, suggesting that the primary pathway for DCO^+ production would be through $H_2D^+ + CO$ (N. T. Phuong et al. 2018). On the other hand, N_2H^+ formed through protonation of N_2 will be readily destroyed in the presence of CO, which will cause a rapid decrease in the N_2H^+ abundance as seen in Figure 2.

5.4. Temperature Trends in the Ring Region

The DISKFIT analysis of our observations of N_2H^+ (4–3) and DCO^+ (5–4) along with the NOEMA observations of N_2H^+ (1–0) and DCO^+ (1–0, 3–2) by N. T. Phuong et al. (2018, 2021) indicate that N_2H^+ and DCO^+ are best represented by average temperatures of 12 and 16 K (Table 4), respectively. These rotation temperatures are consistent with N_2H^+ being located closer to the cold disk midplane than DCO^+ and a fortiori, CO and its isotopologues previously studied by N. T. Phuong et al. (2020b).

However, in our chemical model, while the distributions of N_2H^+ and DCO^+ extend to regions with temperatures of 12 and 16 K, their density-weighted average temperatures are 21 K and 24 K, respectively. The discrepancy with the observed temperatures can be attributed to our limited understanding of the physical structure of the ring region and the simplifications applied in the model to derive the physical structure. DCO^+ abundances are sensitive to grain size, and the dust-to-gas mass ratio significantly influences gas-phase molecular abundances. S. Gavino et al. (2021, 2023) recently investigated the impact of the dependence of the grain size on their temperature. They found that large grains exhibit lower temperatures than smaller ones, with an effect on chemistry that cannot be properly represented by a single grain size. This can influence the structure of the CO distribution (with more CO near the midplane) and, consequently, the gas-phase abundances of DCO^+ and N_2H^+ in the densest, coldest regions.

6. Conclusions

In this paper, we have presented high-sensitivity ALMA Band 7 observations of the circumstellar disk around the triple star system GG Tau A, which highlight CO-regulated cold molecular chemistry in the shielded high-density regions near

the disk midplane. Our key findings and conclusions are summarized below.

1. With Band 7 single-pointing observation of GG Tau A, we achieved a spectral resolution of 0.1 km s^{-1} and an angular resolution of 0.″8–0.″9. We spatially resolved the emission from N_2H^+ (4–3) and DCO^+ (5–4) while o–H_2D^+ (1(1, 0)–1(1, 1)), ^{13}CS (8–7), and SO_2 19(4, 16)–19(3, 17) show no detection.
2. Comparing the predictions of a parametric disk model to our observed visibilities along with the lower excitation transition observations obtained with NOEMA by N. T. Phuong et al. (2018) and N. T. Phuong et al. (2020b), we constrain the average temperature of the N_2H^+- and DCO^+-emitting regions to be around 12 K and 16 K, respectively. These are at odds with the predictions from all the chemical models we explored and all the previous studies. Chemical models suggest DCO^+ peaks at 20–25 K, where some CO remains in the gas phase, and N_2H^+ peaks around 20 K, where CO is fully frozen onto grains. On the contrary, our observational constraints indicate that both molecules trace regions below the CO layer (N. T. Phuong et al. 2020a), much closer to the midplane than previously thought, with N_2H^+ being the closest.
3. Our radial distribution of DCO^+ (5–4) emission reveals an atypical partially overlapping double-ring structure. The inner ring peaks at 210 ± 50 au within the continuum ring region, while the more intense outer ring peaks at 375 ± 10 au in the outer disk. We hypothesize that DCO^+ forms via two different pathways in the ring and the outer disk regions depending on the gas-phase CO abundance. In the ring region, DCO^+ forms through isotope exchange after HCO^+ arises from CO protonation. However, constraining DCO^+ formation in the outer disk regions requires future work that takes into account the complex physical structure.
4. N_2H^+ (4–3) emission shows a ring-like radial distribution facilitated through protonation of N_2 with its emission layer situated right below the DCO^+ layer. The anticorrelation between the N_2H^+ distribution and the CO distribution is clearly visible in our modeled simulations.
5. We ran numerous chemical models varying the CRI rates, C/O ratios, and stellar UV fluxes. These models suggest that the chemistry of H_2D^+, N_2H^+, and DCO^+ in cold, dense regions is primarily influenced by the gas-phase CO abundance and the dominant midplane ion, H_3^+. These regions are shielded from external UV radiation, making CRI the most crucial factor in determining the CO and H_3^+ abundances and, consequently, the distributions of N_2H^+, DCO^+, and H_2D^+. On the other hand, the chemistry of ^{13}CS and SO_2 is very sensitive to the C/O ratio.
6. After running a grid of astrochemical models to simultaneously fit the surface density constraints from the observed transitions along with the upper limits provided by the nondetections, our best-fit model, with a C/O ratio of 1.0 and a subinterstellar CRI rate of 10^{-18} s^{-1}, successfully reproduced the radial trends in surface density for DCO^+ but slightly overestimated both the N_2H^+ content and the expected rotation temperatures. The CRI attenuation in the high-density GG Tau A ring can be attributed to an increased number of collisions experienced by cosmic-ray particles as they gyrate toward the midplane.
7. The nondetection of o–H_2D^+ (1(1, 0)–1(1, 1)) suggests that ionization is much lower than the standard interstellar rate in the disk midplane due to its very high density. In the cold midplane region, H_2D^+ is directly dependent on the abundance of H_3^+, which, in turn, is regulated by the ionization rate. The nondetection of H_2D^+ aligns with our best model, where the expected surface density is below our observationally determined 3σ upper limit only for a subinterstellar CRI rate.

The GG Tau A disk is very complex, but it is one of the nearest (hence larger) and more massive disks found around a low-mass star system. Such properties should facilitate the detection of o–H_2D^+ (1(1, 0)–1(1, 1)). However, its modeled surface density being close to the observationally constrained 3σ upper limit suggests that the detection of H_2D^+ is within ALMA's capabilities, although at the cost of a significantly longer integration time.

Acknowledgments

This paper makes use of the following ALMA data: ADS/JAO ALMA #2021.1.00342.S. ALMA is a partnership of ESO (representing its member states), NSF (USA) and NINS (Japan), together with NRC (Canada), MOST and ASIAA (Taiwan), and KASI (Republic of Korea), in cooperation with the Republic of Chile. The Joint ALMA Observatory is operated by ESO, AUI/NRAO, and NAOJ. The National Radio Astronomy Observatory is a facility of the National Science Foundation operated under a cooperative agreement by Associated Universities, Inc. L.M. acknowledges the financial support of DAE and DST-SERB research grants (SRG/2021/002116 and MTR/2021/000864) of the Government of India. A.D. and S.G. thank the French CNRS programs PNP, PNPS, and PCMI. This research was carried out in part at the Jet Propulsion Laboratory, which is operated for NASA by the California Institute of Technology. K.W. acknowledges the financial support from the NASA Emerging Worlds grant 18-EW-182-0083. Th.H. and D.S. acknowledge support from the European Research Council under the Horizon 2020 Framework Program via the ERC Advanced Grant Origins 83 24 28 (PI: Th. Henning). N.T. P. acknowledges the financial support of Vingroup Innovation Foundation (VINIF) under project code VINIF.2023.DA.057″. A.C. received financial support from the European Research Council (ERC) under the European Union's Horizon 2020 research and innovation program (ERC Starting Grant "Chemtrip," grant agreement No 949278). R.S. thanks NASA for financial support through various Astrophysics Data Program awards. A.K. acknowledges support from the NKFIH excellence grant TKP2021-NKTA-64. We would like to thank the anonymous referees for their constructive comments, which helped improve the manuscript.

Facility: ALMA.

Software: `CASA` (J. P. McMullin et al. 2007), `keplerian_mask` (R. Teague 2020), `GoFish` (R. Teague 2019), `VISIBLE` (R. A. Loomis et al. 2018b), `dynesty` (J. S. Speagle 2020), IMAGER (https://imager.oasu.u-bordeaux.fr), `DNAUTILUS` (L. Majumdar et al. 2017), `numpy` (C. R. Harris et al. 2020), astropy (Astropy Collaboration et al. 2013, 2018, 2022), `matplotlib` (J. D. Hunter 2007).

Appendix A
Channel Maps, Moment Maps, and Radial Profiles

The generated channel maps for the detected transitions, N_2H^+ (4–3) and DCO^+ (5–4), are shown in Figures A1 and A2,

respectively. Figure A3 shows integrated intensity maps between the velocity range 5.0 and 8.0 km s^{-1} for all the targeted transitions. Sigma clipping and masking are not performed while generating these integrated intensity maps. Figure A4 shows the radial distribution of azimuthally averaged emission for the targeted transitions and the continuum generated from the integrated intensity maps shown in Figure A3. We have displayed the matched filter responses for all the targeted transitions in Figure A5. The methods for generating all these figures are explained in Section 2.2.

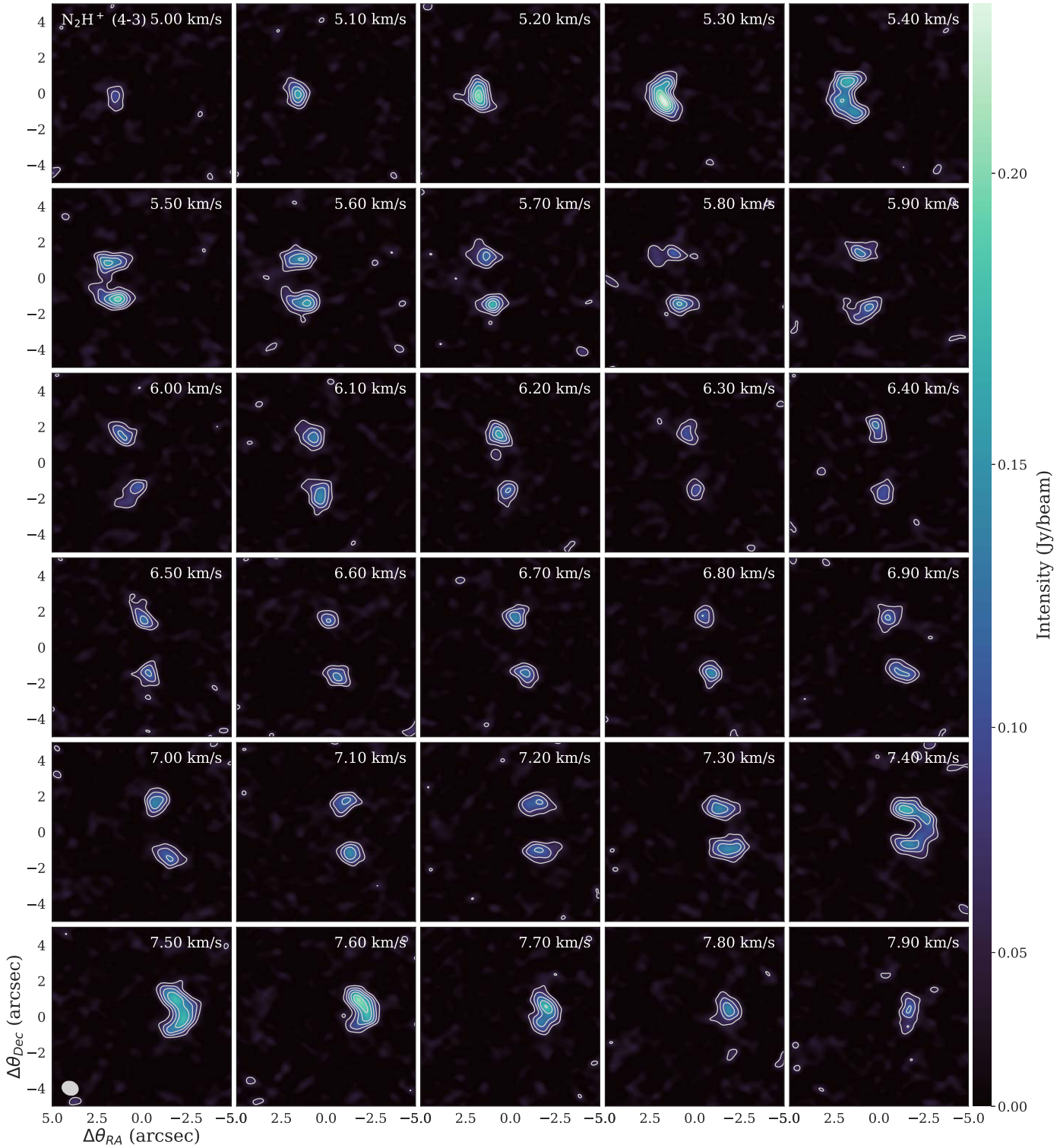

Figure A1. Channel maps of N_2H^+ (4–3) imaged with the `tclean` task in CASA as explained Section 2. The channel velocities (LSRK) are displayed in the top right corner of each channel in units of km s^{-1}. The solid contours are [3, 5, 7, 9,...] × σ levels, where σ = 14.6 mJy $beam^{-1}$. The ellipse at the lower left corner indicates the beam size of $0\overset{''}{.}93 \times 0.''77$ with a PA of $68\overset{\circ}{.}76$. The color bar is stretched nonlinearly to showcase the line emissions more prominently.

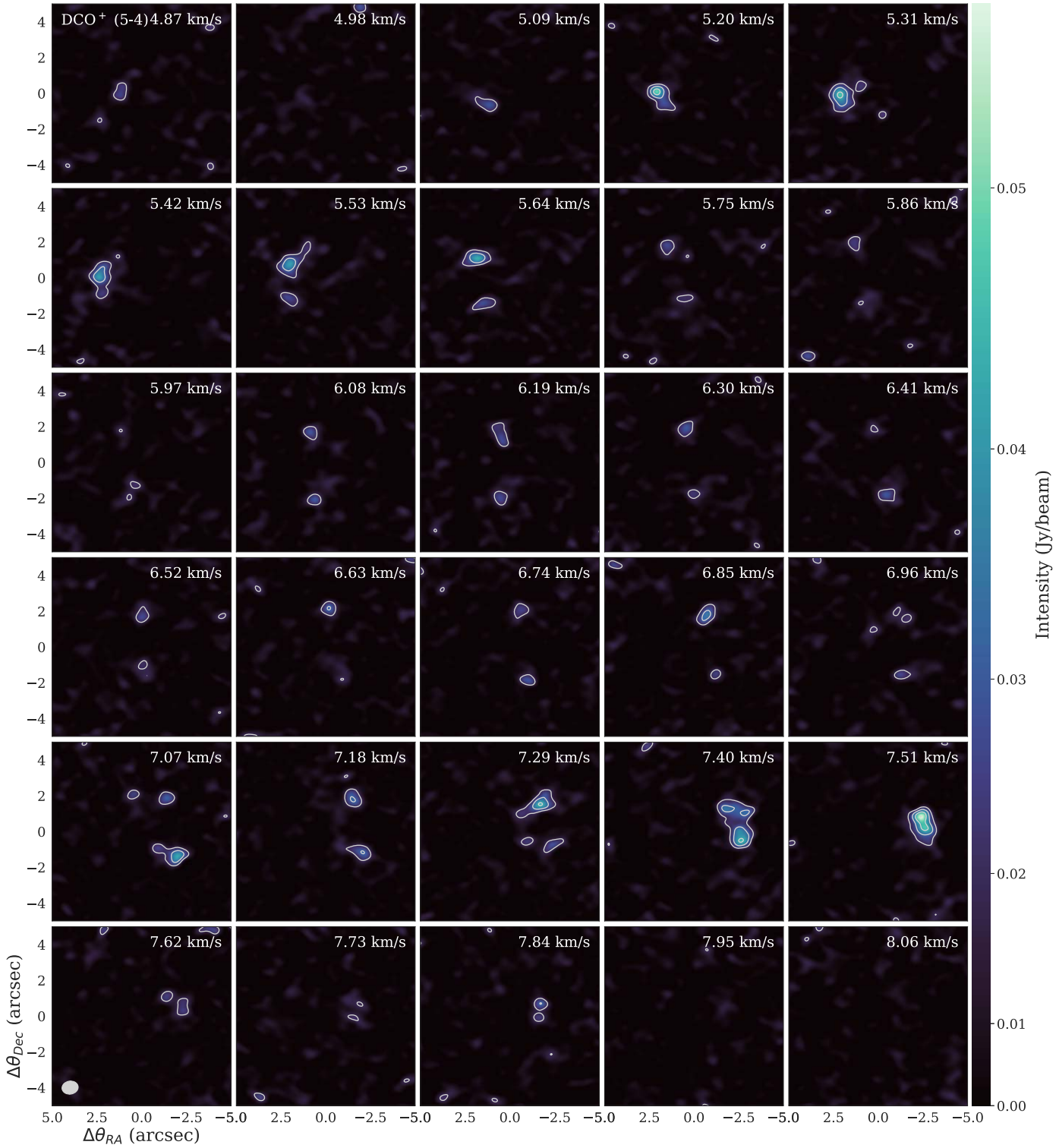

Figure A2. Channel maps of DCO^+ (5–4) imaged with the `tclean` task in CASA as explained Section 2. The channel velocities (LSRK) are displayed in the top right corner of each channel in units of km s^{-1}. The solid contours are [3, 5, 7, 9,...] $\times \sigma$ levels, where $\sigma = 5.6$ mJy $beam^{-1}$. The ellipse at the lower left corner indicates the beam size of $0\farcs91 \times 0\farcs73$ with a PA of $99\fdg20$. The color bar is stretched nonlinearly to showcase the line emissions more prominently.

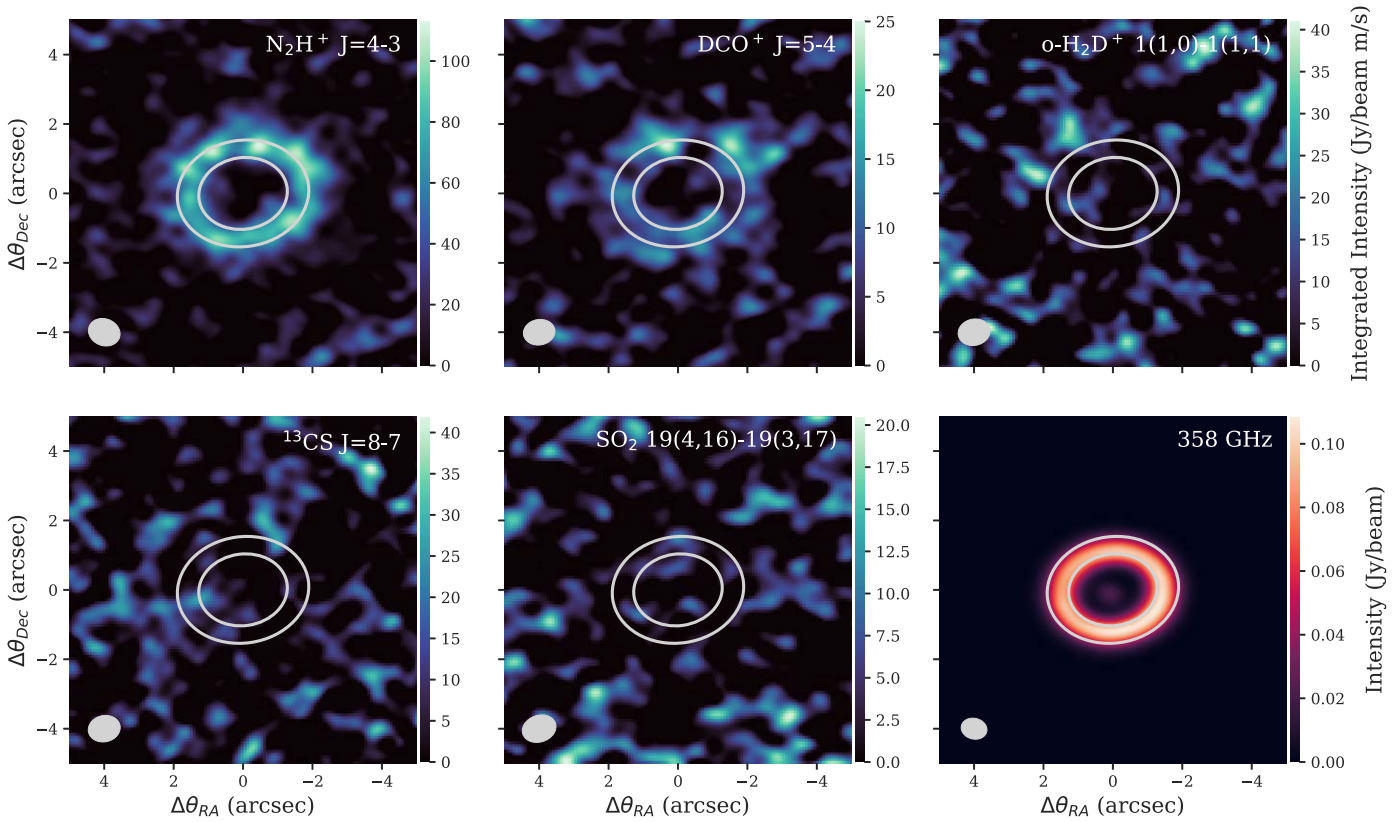

Figure A3. Integrated intensity maps of the targeted transitions generated without sigma clipping and masking. The overplotted elliptical ring contours in the white are at 193 and 285 au to indicate the continuum ring region where 90% of the circumtertiary emission arises (S. Guilloteau et al. 1999). The panel at the bottom right corner is the continuum image at 358 GHz.

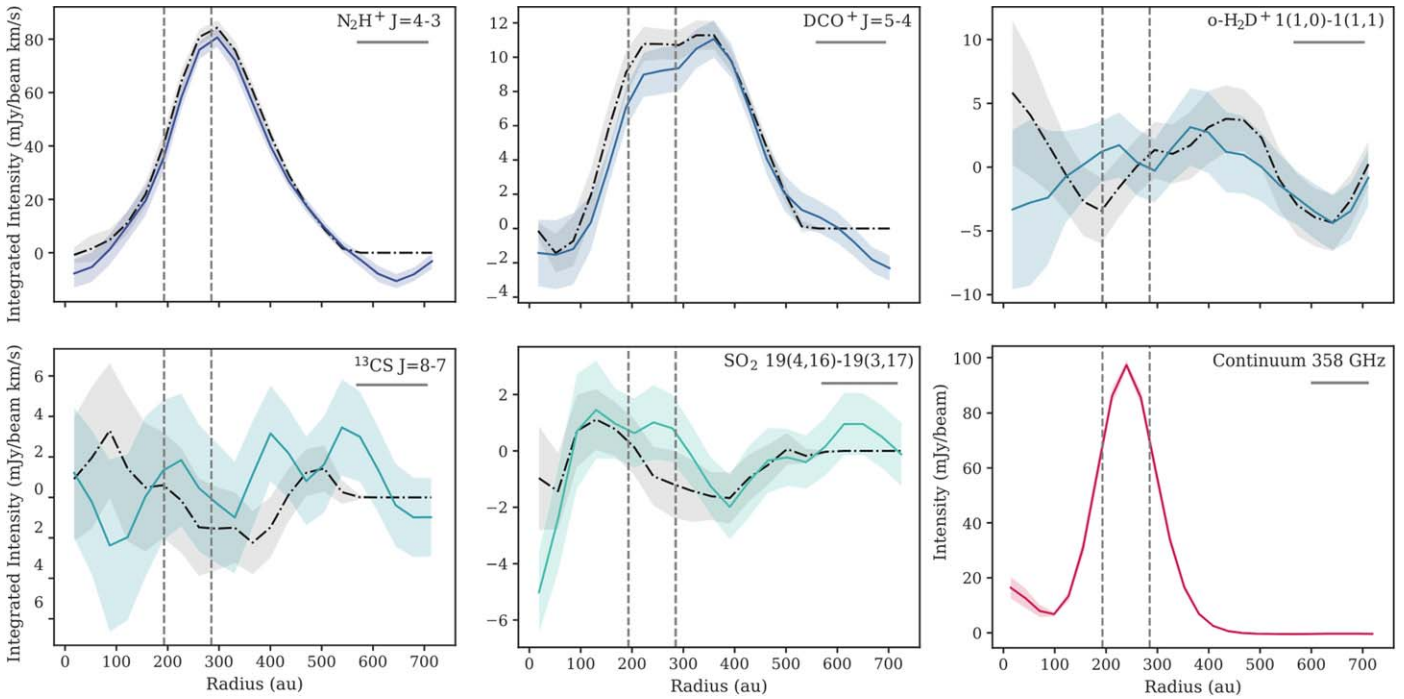

Figure A4. The dashed dot and solid curves represent azimuthally averaged velocity-integrated radial profiles generated from integrated intensity maps with and without Keplerian masking, respectively. The shaded region in the above figure corresponds to 1σ rms. The gray horizontal line at the top right denotes the beam major axis. The dashed vertical lines are to designate the location of the ring around GG Tau A, spanning from 193 to 285 au. The subplot at the bottom right corner is the radial distribution of the azimuthally averaged continuum emission at 358 GHz.

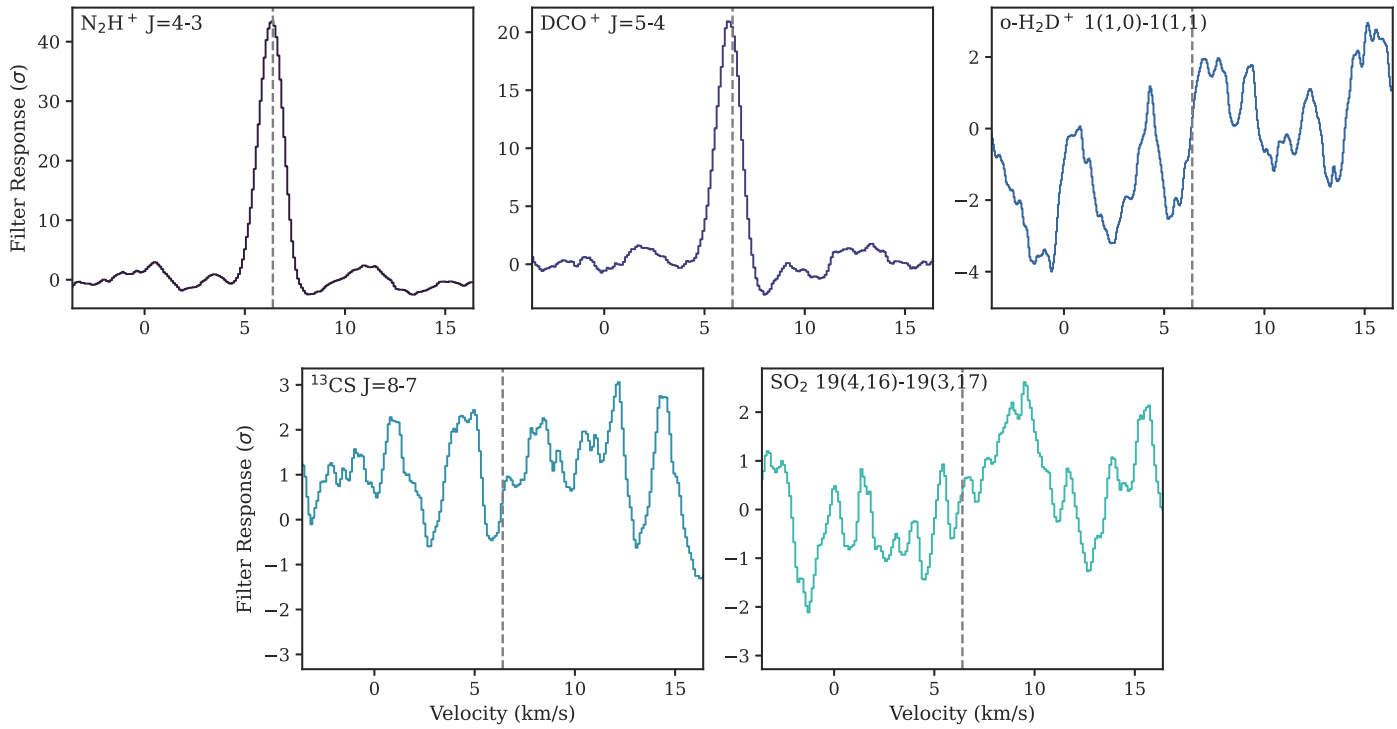

Figure A5. Matched filter responses to the emission for the targeted transitions, written at the upper left corner. The vertical gray dashed line is plotted at source velocity $v_{\rm LSRK} = 6.4$ km s^{-1} for each subplot. Only N_2H^+ (4–3) and DCO^+ (5–4) show clear detections; the rest of them do not.

Appendix B
IMAGER and DISKFIT Analysis

Figure B1 shows the Keplerian deprojection produced by the IMAGER command `KEPLER`. Images used for this purpose were produced with IMAGER and have an angular resolution of $0.''66 \times 0.''53$ at a PA of 83°. Spectral resolution prior to Keplerian velocity correction was about 0.1 km s^{-1}. This correction requires resampling of the spectra on a different grid, which results in correlated channels; the correlation factor is estimated from the noise autocorrelation spectrum. The best-fit radial profile derived from DISKFIT is always slightly above the measured one because the deconvolution with a limited signal-to-noise ratio cannot recover the full line brightness, while the *uv* plane fitting method is not biased in this respect.

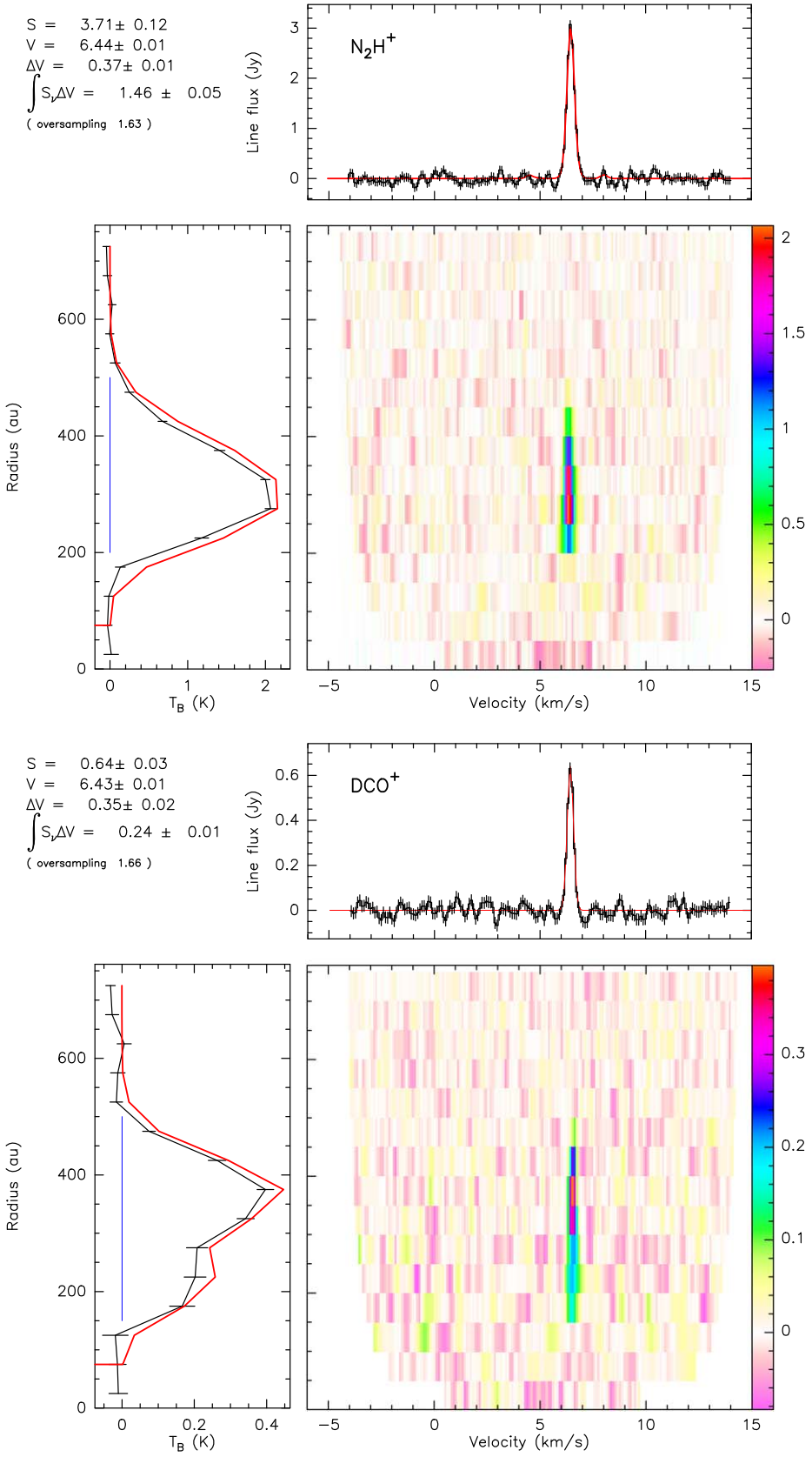

Figure B1. Kepler plots generated for the observed transitions of N_2H^+ (4–3) (top) and DCO^+ (5–4) (bottom). For each molecule, the map is the brightness temperature (in units of K) as a function of velocity and radius ("teardrop" plot). The left panel shows the peak brightness radial profile, with error bars indicated, and the red profile is the one derived from the best-fit DISKFIT model. The top panel shows the integrated spectrum over the range indicated by the blue line in the radial profile, with the best-fit Gaussian spectrum superimposed in red. The peak (S, in units of Jy) and integrated ($\int S_\nu dV$, in units of Jy km s^{-1}) flux densities, central velocity (V, in units of km s^{-1}), and FWHM line width (ΔV, in units of km s^{-1}) obtained from a Gaussian fit to the integrated spectrum are given in the upper left corner of each panel.

Appendix C
Simple Local Thermodynamic Equilibrium Approach

We have undertaken a simpler approach to calculate disk-averaged surface densities where we assume LTE considering the disk densities are relatively high compared to critical densities for the studied transitions. This method requires prior knowledge of rotational temperature for a single transition.

For optically thin emission, the surface density of molecules in the upper state of a specific transition is expressed as

$$N_u^{\rm thin} = \frac{4\pi}{hcA_{ul}}\frac{\left(\int S_\nu dv\right)}{\Omega}, \tag{C1}$$

$$= \frac{8\pi k\nu^2}{hc^3A_{ul}}\left(\int T_b dv\right), \tag{C2}$$

where $\int S_\nu dv$ is the velocity-integrated flux density, A_{ul} is the Einstein coefficient, Ω denotes the solid angle subtended by the emission area, and h and c stand for the Planck constant and the speed of light in a vacuum, respectively (P. F. Goldsmith & W. D. Langer 1999). In the alternate form, ν is the line frequency and T_b is the line brightness temperature.

The total surface density can be derived from the upper state surface density, assuming a Boltzmann distribution

$$N_T^{\rm thin} = N_u^{\rm thin}\frac{Q(T_{\rm rot})}{g_u}\exp\left(\frac{E_u}{T_{\rm rot}}\right), \tag{C3}$$

where g_u is the degeneracy, E_u is the energy of the upper energy level in units of K, and $Q(T_{\rm rot})$ is the partition function at the rotation temperature $T_{\rm rot}$, which can be computed by summation over the energy levels or by interpolating tabulated Q values for discrete $T_{\rm rot}$ values found in the Cologne Database for Molecular Spectroscopy (C. P. Endres et al. 2016).

If the transition is optically thick, the above value gives a strict lower limit to the observed surface density. Opacity corrections are possible in a purely homogeneous medium with only turbulent or thermal line broadening (P. F. Goldsmith & W. D. Langer 1999)

$$N_T = N_T^{\rm thin}\frac{\tau}{1-e^{-\tau}}, \tag{C4}$$

where we can self-consistently calculate the optical depth, τ assuming a Gaussian-like line profile $\sim 1/\Delta v$ at the line center (P. F. Goldsmith & W. D. Langer 1999), $\Delta v = 0.25$ km s^{-1} being the intrinsic FWHM line width constrained from the DISKFIT analysis

$$\tau = \frac{A_{ul}c^3}{8\pi\nu^3\Delta v}N_u\left[\exp\left(\frac{h\nu}{kT_{\rm rot}}\right)-1\right]. \tag{C5}$$

Unfortunately, in our case, the abovementioned correction does not hold while calculating the radially resolved surface density, even if we apply this to radially dependent emission. Because of the Keplerian shear, there are significant regions in our images where the line-of-sight opacity varies both as a function of azimuth and radius, with both directions being insufficiently well resolved at our angular resolution (about 100 au). Accordingly, the azimuthally averaged brightness does not originate from a unique opacity below about 400 au.

However, the effect is expected to be small. The peak brightness of N_2H^+ (see Figure B1) is 2 K, while the brightness temperature of an optically thick line would be $J_\nu(T_{\rm rot}) = 5.3$ K for $T_{\rm rot} = 12$ K at the $J = 4$–3 line frequency. This indicates a peak line opacity of about 0.47, leading to a $\sim$22% opacity correction at most. For DCO^+, whose emission is about 3 times fainter, the correction is even smaller, as for the (undetected) emission from H_2D^+ and other molecules. We thus expect the constraint given by the optically thin approximation to be a reasonable estimate for the mean surface density.

We explore the likely ranges of disk-averaged surface density using nested sampling while assuming lognormal priors for both the molecules in the range $10^5 < N_T < 10^{18}$ cm^{-2} and fixing the rotational temperature to the values constrained in the DISKFIT analysis. The rotation temperatures for N_2H^+ and DCO^+ were set at 12 K and 16 K, respectively. A value of 15 K was used for the undetected molecules. The Python

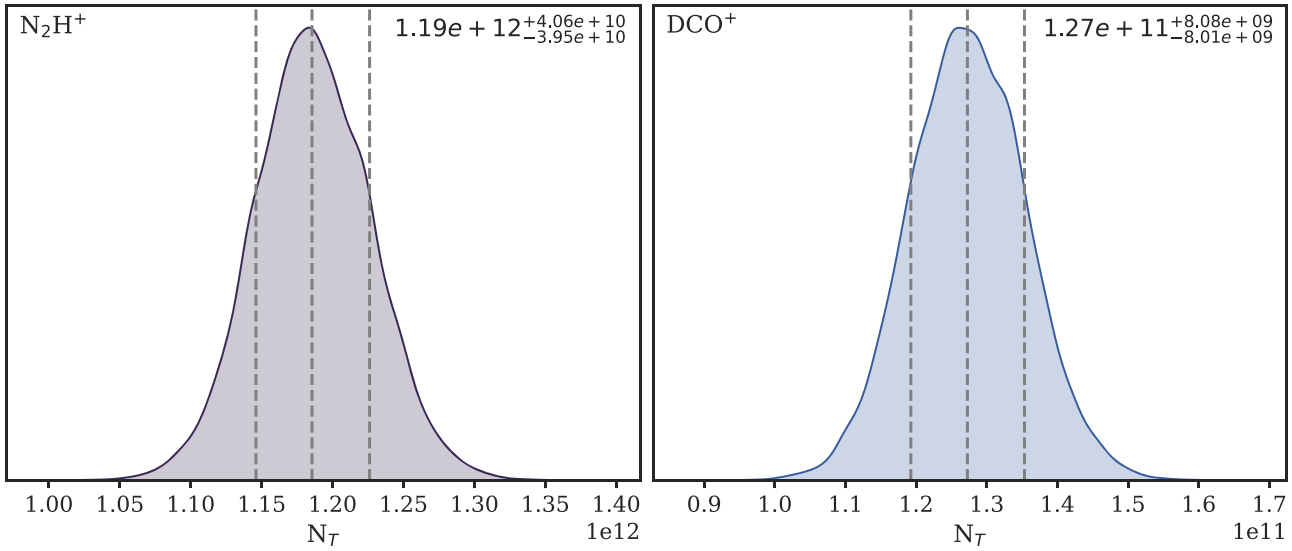

Figure C1. Posterior distributions for disk-averaged surface density calculations using the simple LTE approach. The left panel is for the molecule N_2H^+, and the right one is for DCO^+. The gray dashed lines represent 16th, 50th, and 84th percentiles of the distribution. The median value with 1σ error bars (68% confidence interval) are reported at the top right.

package utilized to sample the posterior distribution is `dynesty` (J. S. Speagle 2020). We consider the median of the posterior as the best-fit value, while the 16th and 84th percentile values account for the 1σ uncertainties. Posterior distributions for these averaged surface density derivations are shown in Figure C1.

Appendix D
Grids of Astrochemical Models and Finding the Best-fit Model

We ran a large number of astrochemical models with various combinations of parameters. The grids of models are summarized in Table 8. Note that we have not implemented any grain growth in our models due to poor constraints on larger grain sizes. We explored the parameter space using the least squares method while simultaneously considering the observational constraints on the surface densities for N_2H^+ and DCO^+ from our observations and ^{13}CS as reported by N. T. Phuong et al. (2021). We ensured that the modeled values for undetected molecules remained below their respective upper limits. To quantify the goodness of fit, we calculated reduced chi-squared values. This metric evaluates the agreement between the observed and modeled surface densities across multiple molecules and radii. The reduced chi-squared calculation is defined as follows

$$\chi^2_{\rm red} = \frac{1}{\nu}\sum_j\left(\sum_i\left(\frac{N_{\rm obs}(i,j) - N_{\rm model}(i,j)}{\sigma_{\rm obs}(i,j) + \sigma_{\rm model}(i,j)}\right)^2\right). \quad \text{(D1)}$$

In the equation, ν, the number of degrees of freedom is 25. $N_{\rm obs}(i, j)$ and $N_{\rm model}(i, j)$ denote the observed and modeled surface densities of the jth molecule at the ith radial point, respectively. The terms $\sigma_{\rm obs}(i, j)$ and $\sigma_{\rm model}(i, j)$ represent the associated error estimates for the observed and modeled values, respectively. Observational errors were derived from the error bars in the peak column density values in Table 4, while the modeled errors were assumed to be 20% to account for uncertainties in the chemical models due to rate coefficients and other chemical parameters. The best-fit model is the one with the lowest $\chi^2_{\rm red}$ value. Although $\chi^2_{\rm red}$ depends on the assumed errors, the best-fit solution was found to be independent of this assumption.

Table 8
Parameter Space Explored with DNAUTILUS

Initial Abundances	Settling	Grain Growth	$f_{\rm UV,\ 214\ au}$ (χ_0)[a]	C/O[b]	$\zeta_{\rm CR}$[c] (s^{-1})
Atomic[d]	no	no	375, 1500, 3000	0.5, 0.7, 0.9, 1.0, 1.2	10^{-16}, 10^{-17}, 10^{-18}, 10^{-19}, 10^{-20}
10^6 yr Molecular Cloud[e]	no	no	375, 1500, 3000	0.5, 0.7, 0.9, 1.0, 1.2	10^{-16}, 10^{-17}, 10^{-18}, 10^{-19}, 10^{-20}
Atomic[d]	yes	no	375, 1500, 3000	0.5, 0.7, 0.9, 1.0, 1.2	10^{-16}, 10^{-17}, 10^{-18}, 10^{-19}, 10^{-20}
10^6 yr Molecular Cloud[e]	yes	no	375, 1500, 3000	0.5, 0.7, 0.9, 1.0, 1.2	10^{-16}, 10^{-17}, 10^{-18}, 10^{-19}, 10^{-20}

Notes.
[a] $f_{\rm UV}$ is the stellar UV flux at the reference radius, 214 au in the units of the Draine interstellar UV field, χ_0.
[b] C/O ratios have been considered around the standard value of 0.7 to account for low depletion and high depletion of oxygen (L. Reboussin et al. 2015).
[c] Different CRI rates $\zeta_{\rm CR}$ have been explored to account for how they impact our chemistry.
[d] In the reset scenario, we have taken our initial abundances in atomic forms along with H_2 and HD and run our astrochemical model for 10^6 yr.
[e] We have also considered the inheritance scenario as another possibility, where we have run a cloud model with atomic initial abundances, and the final abundances after 10^6 yr are used as the initial abundance in the disk model. The disk model was then run for 10^6 yr.

ORCID iDs

Parashmoni Kashyap https://orcid.org/0009-0008-2350-5876
Liton Majumdar https://orcid.org/0000-0001-7031-8039
Anne Dutrey https://orcid.org/0000-0003-2341-5922
Stéphane Guilloteau https://orcid.org/0000-0003-3773-1870
Karen Willacy https://orcid.org/0000-0001-6124-5974
Edwige Chapillon https://orcid.org/0009-0003-6480-8084
Richard Teague https://orcid.org/0000-0003-1534-5186
Dmitry Semenov https://orcid.org/0000-0002-3913-7114
Thomas Henning https://orcid.org/0000-0002-1493-300X
Neal Turner https://orcid.org/0000-0001-8292-1943
Raghvendra Sahai https://orcid.org/0000-0002-6858-5063
Ágnes Kóspál https://orcid.org/0000-0001-7157-6275
Audrey Coutens https://orcid.org/0000-0003-1805-3920
V. Piétu https://orcid.org/0009-0006-3497-397X
Pierre Gratier https://orcid.org/0000-0002-6636-4304
Maxime Ruaud https://orcid.org/0000-0003-0522-5789
N. T. Phuong https://orcid.org/0000-0002-4372-5509
E. Di Folco https://orcid.org/0009-0009-9618-4927
Chin-Fei Lee https://orcid.org/0000-0002-3024-5864
Y.-W. Tang https://orcid.org/0000-0002-0675-276X

References

Aikawa, Y., van Zadelhoff, G. J., van Dishoeck, E. F., & Herbst, E. 2002, A&A, 386, 622
Anderson, D. E., Cleeves, L. I., Blake, G. A., et al. 2022, ApJ, 927, 229
Andrews, S. M., Chandler, C. J., Isella, A., et al. 2014, ApJ, 787, 148
Astropy Collaboration, Price-Whelan, A. M., Lim, P. L., et al. 2022, ApJ, 935, 167
Astropy Collaboration, Price-Whelan, A. M., Sipőcz, B. M., et al. 2018, AJ, 156, 123
Astropy Collaboration, Robitaille, T. P., Tollerud, E. J., et al. 2013, A&A, 558, A33
Bergin, E. A., Alves, J., Huard, T., & Lada, C. J. 2002, ApJL, 570, L101
Boogert, A. C. A., Gerakines, P. A., & Whittet, D. C. B. 2015, ARA&A, 53, 541
Brauer, R., Pantin, E., Di Folco, E., et al. 2019, A&A, 628, A88
Caselli, P., Vastel, C., Ceccarelli, C., et al. 2008, A&A, 492, 703
Caselli, P., Walmsley, C. M., Tafalla, M., Dore, L., & Myers, P. C. 1999, ApJL, 523, L165
Cataldi, G., Yamato, Y., Aikawa, Y., et al. 2021, ApJS, 257, 10
Ceccarelli, C., Caselli, P., Bockelée-Morvan, D., et al. 2014, in Protostars and Planets VI, ed. H. Beuther et al. (Tucson, AZ: Univ. of Arizona Press), 859
Ceccarelli, C., Dominik, C., Lefloch, B., Caselli, P., & Caux, E. 2004, ApJL, 607, L51
Chapillon, E., Parise, B., Guilloteau, S., & Du, F. 2011, A&A, 533, A143
Cleeves, L. I., Adams, F. C., & Bergin, E. A. 2013, ApJ, 772, 5
Cleeves, L. I., Bergin, E. A., Qi, C., Adams, F. C., & Öberg, K. I. 2015, ApJ, 799, 204
Dartois, E., Dutrey, A., & Guilloteau, S. 2003, A&A, 399, 773
Draine, B. T. 1978, ApJS, 36, 595
Drozdovskaya, M. N., Walsh, C., van Dishoeck, E. F., et al. 2016, MNRAS, 462, 977
Du, F., & Bergin, E. A. 2014, ApJ, 792, 2
Dutrey, A., di Folco, E., Guilloteau, S., et al. 2014, Natur, 514, 600
Dutrey, A., Henning, T., Guilloteau, S., et al. 2007, A&A, 464, 615
Endres, C. P., Schlemmer, S., Schilke, P., Stutzki, J., & Müller, H. S. P. 2016, JMoSp, 327, 95
Gaia Collaboration, Brown, A. G. A., Vallenari, A., et al. 2018, A&A, 616, A1
Gaia Collaboration, Prusti, T., de Bruijne, J. H. J., et al. 2016, A&A, 595, A1
Gammie, C. F. 1996, ApJ, 457, 355
Gavino, S., Dutrey, A., Wakelam, V., et al. 2021, A&A, 654, A65
Gavino, S., Kobus, J., Dutrey, A., et al. 2023, A&A, 680, A59
Goldsmith, P. F., & Langer, W. D. 1999, ApJ, 517, 209
Graedel, T. E., Langer, W. D., & Frerking, M. A. 1982, ApJS, 48, 321
Guilloteau, S., Dutrey, A., & Simon, M. 1999, A&A, 348, 570
Harris, C. R., Millman, K. J., van der Walt, S. J., et al. 2020, Natur, 585, 357
Huang, J., Öberg, K. I., Qi, C., et al. 2017, ApJ, 835, 231
Hunter, J. D. 2007, CSE, 9, 90
Jenkins, E. B. 2009, ApJ, 700, 1299
Kataoka, A., Tanaka, H., Okuzumi, S., & Wada, K. 2013, A&A, 554, A4
Le Gal, R., Öberg, K. I., Teague, R., et al. 2021, ApJS, 257, 12
Loomis, R. A., Öberg, K. I., Andrews, S. M., et al. 2018a, AJ, 155, 182
Loomis, R. A., Oberg, K. I., Andrews, S. M., et al., 2018b VISIBLE: VISIbility Based Line Extraction, Astrophysics1133 Source Code Library, ascl:1802.006
Lynden-Bell, D., & Pringle, J. E. 1974, MNRAS, 168, 603
Majumdar, L., Gratier, P., Ruaud, M., et al. 2017, MNRAS, 466, 4470
Mathews, G. S., Klaassen, P. D., Juhász, A., et al. 2013, A&A, 557, A132
McMullin, J. P., Waters, B., Schiebel, D., Young, W., & Golap, K. 2007, in ASP Conf. Ser. 376, Astronomical Data Analysis Software and Systems XVI, ed. R. A. Shaw, F. Hill, & D. J. Bell (San Francisco, CA: ASP), 127
Neufeld, D. A., Wolfire, M. G., & Schilke, P. 2005, ApJ, 628, 260
Öberg, K. I., & Bergin, E. A. 2021, PhR, 893, 1
Öberg, K. I., Furuya, K., Loomis, R., et al. 2015, ApJ, 810, 112
Öberg, K. I., Qi, C., Wilner, D. J., & Andrews, S. M. 2011, ApJ, 743, 152
Öberg, K. I., van Broekhuizen, F., Fraser, H. J., et al. 2005, ApJL, 621, L33
Okuzumi, S., Tanaka, H., Kobayashi, H., & Wada, K. 2012, ApJ, 752, 106
Padovani, M., Hennebelle, P., & Galli, D. 2013, A&A, 560, A114
Padovani, M., Ivlev, A. V., Galli, D., & Caselli, P. 2018, A&A, 614, A111
Phuong, N. T., Chapillon, E., Majumdar, L., et al. 2018, A&A, 616, L5
Phuong, N. T., Dutrey, A., Chapillon, E., et al. 2021, A&A, 653, L5
Phuong, N. T., Dutrey, A., Di Folco, E., et al. 2020a, A&A, 635, L9
Phuong, N. T., Dutrey, A., Diep, P. N., et al. 2020b, A&A, 635, A12
Piétu, V., Dutrey, A., & Guilloteau, S. 2007, A&A, 467, 163
Qi, C., Öberg, K. I., Wilner, D. J., et al. 2013, Sci, 341, 630
Qi, C., Wilner, D. J., Aikawa, Y., Blake, G. A., & Hogerheijde, M. R. 2008, ApJ, 681, 1396
Reboussin, L., Wakelam, V., Guilloteau, S., Hersant, F., & Dutrey, A. 2015, A&A, 579, A82
Roberts, H., & Millar, T. J. 2000, A&A, 361, 388
Ruaud, M., Gorti, U., & Hollenbach, D. J. 2022, ApJ, 925, 49
Semenov, D., Favre, C., Fedele, D., et al. 2018, A&A, 617, A28
Sipilä, O., Harju, J., & Caselli, P. 2017, A&A, 607, A26
Speagle, J. S. 2020, MNRAS, 493, 3132
Tang, Y.-W., Dutrey, A., Guilloteau, S., et al. 2016, ApJ, 820, 19
Taniguchi, K., Rayalacheruvu, P., Yonetsu, T., et al. 2024, ApJ, 963, 12
Teague, R. 2019, JOSS, 4, 1632
Teague, R. 2020, richteague/keplerian_mask: Initial Release v1.0, Zenodo, doi:10.5281/ZENODO.4321137
Teague, R., & Foreman-Mackey, D. 2018, RNAAS, 2, 173
Teague, R., Semenov, D., Guilloteau, S., et al. 2015, A&A, 574, A137
Thi, W. F., van Zadelhoff, G. J., & van Dishoeck, E. F. 2004, A&A, 425, 955
Wagenblast, R., & Hartquist, T. W. 1989, MNRAS, 237, 1019
Wakelam, V., Chapillon, E., Dutrey, A., et al. 2019, MNRAS, 484, 1563
Wakelam, V., & Herbst, E. 2008, ApJ, 680, 371
Wakelam, V., Ruaud, M., Hersant, F., et al. 2016, A&A, 594, A35
Walsh, C., Nomura, H., Millar, T. J., & Aikawa, Y. 2012, ApJ, 747, 114
Willacy, K. 2007, ApJ, 660, 441
Williams, J. P., & Best, W. M. J. 2014, ApJ, 788, 59
Wootten, A. 1987, in IAU Symp. 120, Astrochemistry, ed. M. Vardya & S. Tarafdar (Dordrecht: Reidel), 311